

2 **RESEARCH**

3 **Modelling the cell-type specific mesoscale murine connectome with  
4 anterograde tracing experiments**

5 **Samson Koelle**<sup>1,2</sup>, **Dana Mastrovito**<sup>1</sup>, **Jennifer D Whitesell**<sup>1</sup>, **Karla E Hirokawa**<sup>1</sup>, **Hongkui Zeng**<sup>1</sup>, **Marina Meila**<sup>2</sup>, **Julie A  
6 Harris**<sup>1</sup>, **Stefan Mihalas**<sup>1</sup>

7 <sup>1</sup>Allen Institute for Brain Science, Seattle, WA, USA

8 <sup>2</sup>Department of Statistics, University of Washington, Seattle, WA, USA

9 **Keywords:** [Connectivity, Cell-type, Mouse]

## ABSTRACT

10 The Allen Mouse Brain Connectivity Atlas consists of anterograde tracing experiments targeting  
11 diverse structures and classes of projecting neurons. Beyond regional anterograde tracing done in  
12 C57BL/6 wild type mice, a large fraction of experiments are performed using transgenic Cre-lines.  
13 This allows access to cell-class specific whole brain connectivity information, with class defined by  
14 the transgenic lines. However, even though the number of experiments is large, it does not come close  
15 to covering all existing cell classes in every area where they exist. Here, we study how much we can fill  
16 in these gaps and estimate the cell-class specific connectivity function given the simplifying  
17 assumptions that nearby voxels have smoothly varying projections, but that these projection tensors  
18 can change sharply depending on the region and class of the projecting cells.

19 This paper describes the conversion of Cre-line tracer experiments into class-specific connectivity  
20 matrices representing the connection strengths between source and target structures. We introduce  
21 and validate a novel statistical model for creation of connectivity matrices. We extend the

22 Nadaraya-Watson kernel learning method which we previously used to fill in spatial gaps to also fill in  
23 a gaps in cell-class connectivity information. To do this, we construct a "cell-class space" based on  
24 class-specific averaged regionalized projections and combine smoothing in 3D space as well as in this  
25 abstract space to share information between similar neuron classes. Using this method we construct a  
26 set of connectivity matrices using multiple levels of resolution at which discontinuities in connectivity  
27 are assumed. We show that the connectivities obtained from this model display expected cell-type  
28 and structure specific connectivities. We also show that the wild type connectivity matrix can be  
29 factored using a sparse set of factors, and analyze the informativeness of this latent variable model.

## AUTHOR SUMMARY

30 Large-scale studies have described the connections between areas in multiple mammalian models in  
31 ever expanding detail. Standard connectivity studies focus on the connection strength between areas.  
32 However, when describing functions at a local circuit level, there is an increasing focus on cell types.  
33 We have recently described the importance of connection types in the cortico-thalamic system, which  
34 allows an unsupervised discovery of its hierarchical organization. In this study we focus on adding a  
35 dimension of connection type for a brain-wide mesoscopic connectivity model. Even with our  
36 relatively massive dataset, the data in the cell type direction for connectivity is quite sparse, and we  
37 had to develop methods to more reliably extrapolate in such directions, and to estimate when such  
38 extrapolations are impossible. This allows us to fill in such a connection type specific inter-areal  
39 connectivity matrix to the extent our data allows. While analyzing this complex connectivity, we  
40 observed that it can be described via a small set of factors. While not complete, this connectivity  
41 matrix represents a a categorical and quantitative improvement in mouse mesoscale connectivity  
42 models.

## 1 INTRODUCTION

43 The mammalian nervous system enables an extraordinary range of natural behaviors, and has  
44 inspired much of modern artificial intelligence. Neural connections from one region to another form  
45 the architecture underlying this capability. These connectivities vary by neuron type, as well as source  
46 cell body location and target axonal projection structures. Thus, characterization of the relationship  
47 between neuron type and source and target structure is important for understanding the overall  
48 nervous system.

49 Viral tracing experiments - in which a viral vector expressing GFP is transduced into neural cells  
50 through stereotaxic injection - are a useful tool for mapping these connections on the mesoscale (???).  
51 The GFP protein moves into the axon of the projecting neurons. The long range connections between  
52 different areas are generally formed by axons which travel from one region to another. Two-photon  
53 tomography imaging can be used to determine the location and strength of the fluorescent signals in  
54 two-dimensional slices. These locations can then be mapped back into three-dimensional space, and  
55 the signal may then be integrated over area into cubic voxels to give a finely-quantized  
56 three-dimensional fluorescence.

57 Several statistical models for the conversion of such experiment-specific signals into generalized  
58 estimates of connectivity strength have been proposed (????). Of these, ? and ? model **regionalized**  
59 **connectivities**, which are voxel connectivities integrated by region. The value of these models is that  
60 they provide some improvement over simply averaging the projection signals of injections in a given  
61 region. However, these previous works only model connectivities observed in wild type mice in which  
62 all neuron types were labeled, and so are poorly suited for extension to tracing experiments that  
63 induce cell-type specific fluorescence (?). In particular, GFP expression is induced by  
64 Cre-recombinase in cell-types specified by transgenic strain. Thus, this paper introduces a **cell**  
65 **class**-specific statistical model to deal with the diverse set of **Cre-lines** described in ?, and expands  
66 this model to the entire mouse brain. In cortex a large number of transgenic lines were chosen for  
67 their laminar specific expression.

68 Our model is a to-our-knowledge novel estimator that takes into account both the spatial position  
69 of the labelled source, as well as the categorical cell class. Like the previously state-of-the-art model in

70 ?, this model predicts regionalized connectivity as an average over positions within the structure, with  
71 nearby experiments given more weight. However, our model weighs class-specific behavior in a  
72 particular structure against spatial position, so a nearby experiment specific to a similar cell-class is  
73 relatively up-weighted, while a nearby experiment specific to a dissimilar class is down-weighted.  
74 This model outperforms the model of ? based on its ability to predict held-out experiments in  
75 leave-one-out cross-validation. We then use the trained model to estimate overall connectivity  
76 matrices for each assayed cell class.

77 The resulting cell-type specific connectivity is a directed weighted multigraph which can be  
78 represented as a tensor with missing values. We do not give an exhaustive analysis of this data, but do  
79 establish a lower-limit of detection, verify several cell-type specific connectivity patterns found  
80 elsewhere in the literature, and show that these cell-type specific signals are behaving in expected  
81 ways. We also decompose the wild type connectivity matrix into factors representing archetypal  
82 connectivity patterns. These components allow approximation of the regionalized connectivity using  
83 a small set of latent components.

84 Section 2 gives information on the data and statistical methodology, and Section 3 presents our  
85 results. These include connectivities, assessments of model fit, and subsequent analyses. Additional  
86 information on our dataset, methods, and results are given in Supplemental Sections 5, ??, and ??,  
87 respectively.

## 2 METHODS

88 We estimate and analyze cell class-specific connectivity functions using models trained on murine  
89 brain viral tracing experiments. This section describes the data used to generate the model, the model  
90 itself, the evaluation of the model against its alternatives, and the use of the model in creation of the  
91 connectivity estimate matrices. It also includes background on the non-negative matrix factorization  
92 method used for decomposing the wild type connectivity matrix into latent factors. Additional  
93 information about our data and methods are given in Supplemental Sections 5 and ??, respectively.

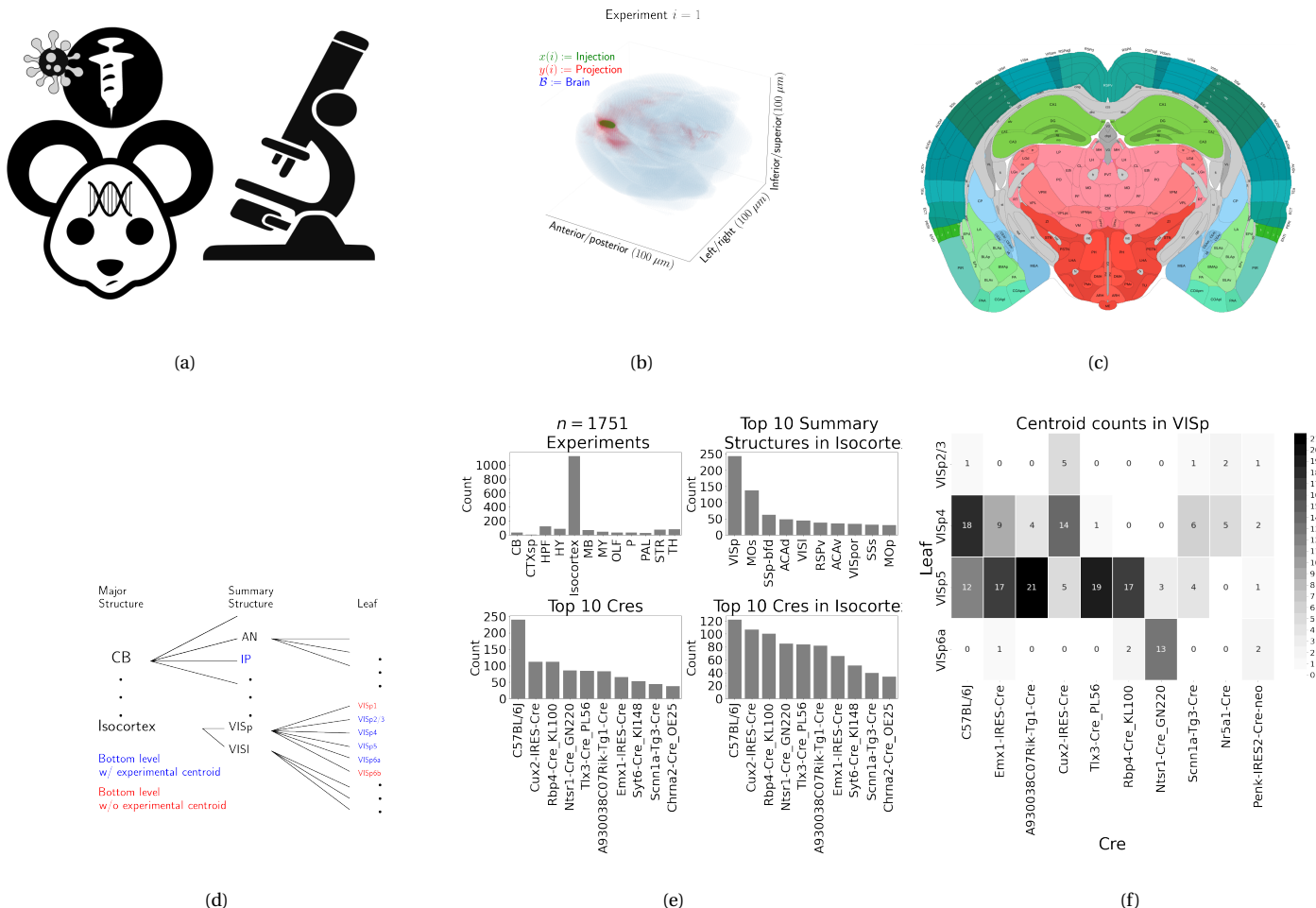


Figure 1: Experimental setting. 1a For each experiment, a Cre-dependent GFP-expressing transgene cassette is transduced by stereotaxic injection into a Cre-driver mouse, followed by serial two-photon tomography imaging. 1b An example of the segmentation of projection (targets) and injection (source) for a single experiment. Within each brain (blue), injection (green) and projection (red) areas are determined via histological analysis and alignment to the Allen Common Coordinate Framework (CCF). 1c Brain region parcellations within a coronal plane of CCFv3. 1d Explanation of nested structural ontology highlighting various levels of CCFv3 structure ontology. Lowest-level (leaf) structures are colored in blue, and structures without an injection centroid are colored in red. 1e Abundances of tracer experiments by Cre-line and region of injection. 1f Co-occurrence of layer-specific centroids and Cre lines within VISp.

<sup>94</sup> **Data**<sup>95</sup> (SK's comment:Update figure to show layer and leaf)

<sup>96</sup> Our dataset  $\mathcal{D}$  consists of  $n = 1751$  publicly available murine brain viral tracing experiments from  
<sup>97</sup> the Allen Mouse Brain Connectivity Atlas. Figure 1a summarizes the experimental process used to  
<sup>98</sup> generate this data. In each experiment, a mouse is injected with an adeno-associated virus (AAV)  
<sup>99</sup> encoding green fluorescent protein (GFP) into a single location in the brain. Location of fluorescence  
<sup>100</sup> is mediated by the location of the injection, the characteristics of the transgene, and the genotype of  
<sup>101</sup> the mouse. In particular, Cre-driver mice are engineered to express Cre under the control of a specific  
<sup>102</sup> and single gene promoter. This localizes expression of Cre to regions with certain transcriptomic  
<sup>103</sup> cell-types signatures. In such Cre-driver mice, we used a double-inverted floxed AAV to produce  
<sup>104</sup> fluorescence that depends on Cre expression in infected cells. To account for the complex cell-type  
<sup>105</sup> targeting induced by a particular combination of Cre-driver genotype and GFP promoter, we refer to  
<sup>106</sup> the combinations of cell-types targeted by a particular combination of AAV and Cre-drive mice as  
<sup>107</sup> cell-classes. For example, we include experiments from Cre-driver lines that selectively label cell  
<sup>108</sup> classes located in distinct cortical layers or other nuclei across the whole brain. By our definition, wild  
<sup>109</sup> type mice transduced with constitutively active GFP promoters induce fluorescence of a particularly  
<sup>110</sup> broad cell class.

<sup>111</sup> For each experiment, the fluorescent signal imaged after injection is aligned into the Allen Common  
<sup>112</sup> Coordinate Framework (CCF) v3, a three-dimensional average template brain that is fully annotated  
<sup>113</sup> with regional parcellations ?. The whole brain imaging and registration procedures described in detail  
<sup>114</sup> in ?? produce quantitative metrics of fluorescence discretized at the  $100 \mu\text{m}$  voxel level. Given an  
<sup>115</sup> experiment, this image was histologically segmented by an analyst into *injection* and *projection* areas  
<sup>116</sup> corresponding to areas containing somas, dendrites and axons or exclusively axons of the transfected  
<sup>117</sup> neurons. An example of a single experiment rendered in 3D is given in Figure 1b. Given an  
<sup>118</sup> experiment  $i$ , we represent injections and projections as functions  $x(i), y(i) : \mathcal{B} \rightarrow \mathbb{R}_{\geq 0}$ , where  
<sup>119</sup>  $\mathcal{B} \subset [1 : 132] \times [1 : 80] \times [1 : 104]$  corresponds to the subset of the  $(1.32 \times 0.8 \times 1.04)$  cm rectangular space  
<sup>120</sup> occupied by the standard voxelized mouse brain. We also calculate injection centroids  $c(i) \in \mathbb{R}^3$  and

121 regionalized projections  $y_{\mathcal{F}}(i) \in \mathbb{R}^T$  given by the sum of  $y(i)$  in each region. A detailed mathematical  
122 description of these steps, including data quality control, is given in Supplemental Section ??.

123 Our goal is the estimation of **regionalized connectivity** from one region to another. A visual  
124 depiction of this region parcellation for a two-dimensional slice of the brain is given in Figure 1c. All  
125 structures annotated in the CCF belong to a hierarchically ordered ontology, with different areas of the  
126 brain are parcellated to differing finer depths within a hierarchical tree. We denote the main levels of  
127 interest as major structures, summary structures, and layers. Not every summary structure has a layer  
128 decomposition within this ontology, so we typically consider the finest possible regionalization - for  
129 example, layer within the cortex, and summary structure within the thalamus, and denote these  
130 structures as leafs. As indicated in Figure 1d, the dataset used to generate the connectivity model  
131 reported in this paper contains certain combinations of region and cell class frequently, and others  
132 not at all. A summary of the most frequently assayed cell classes and structures is given in Figures 1e  
133 and 1f. Since users of the connectivity matrices may be interested in particular combinations, or  
134 interested in the amount of data used to generate a particular connectivity estimate, we present this  
135 information about all experiments in Supplemental Section 5.

136 ***Modeling Regionalized Connectivity***

Cell-class specific connectivity  $f : \mathcal{V} \times \mathbb{R}^3 \times \mathbb{R}^3 \rightarrow \mathbb{R}_{\geq 0}$  gives the directed connection of a particular cell class from one position in the brain to another. In contrast to ?, which only uses wild type C57BL/6J mice, our dataset has experiments targeting  $V = 114$  different combinations of Cre-driver mice and Cre-regulated AAV transgenes jointly denoted as  $\mathcal{V} := \{v\}$ . As in ?, we ultimately estimate an integrated regionalized connectivity defined with respect to a set of  $S = 564$  source leafs  $\mathcal{S} := \{s\}$  and  $T = 1123$  target leafs  $\mathcal{T} := \{t\}$ , of which  $1123 - 564 = 559$  are contralateral. That is, we define

$$\text{regionalized connectivity strength } \mathcal{C} : \mathcal{V} \times \mathcal{S} \times \mathcal{T} \rightarrow \mathbb{R}_{\geq 0} \text{ with } \mathcal{C}(v, s, t) = \sum_{l_j \in s} \sum_{l_{j'} \in t} f(v, l_j, l_{j'}),$$

$$\text{normalized regionalized connectivity strength } \mathcal{C}^N : \mathcal{V} \times \mathcal{S} \times \mathcal{T} \rightarrow \mathbb{R}_{\geq 0} \text{ with } \mathcal{C}^N(v, s, t) = \frac{1}{|s|} \mathcal{C}(v, l_j, l_{j'}),$$

$$\text{normalized regionalized projection density } \mathcal{C}^D : \mathcal{V} \times \mathcal{S} \times \mathcal{T} \rightarrow \mathbb{R}_{\geq 0} \text{ with } \mathcal{C}^D(v, s, t) = \frac{1}{|s||t|} \mathcal{C}(v, l_j, l_{j'})$$

137 where  $l_j$  and  $l_{j'}$  are the locations of source and target voxels, and  $|s|$  and  $|v|$  are defined to be the  
 138 number of voxels in the source and target structure, respectively. Since the normalized strength and  
 139 densities are computable from the strength via a fixed normalization, our main statistical goal is to  
 140 estimate  $\mathcal{C}(v, s, t)$  for all  $v, s$  and  $t$ . In other words, we want to estimate matrices  $\mathcal{C}_v \in \mathbb{R}_{\geq 0}^{S \times T}$ . We call this  
 141 estimator  $\widehat{\mathcal{C}}$ .

Construction of such an estimator raises the questions of what data to use for estimating which connectivity, how to featurize the dataset, what statistical estimator to use, and how to reconstruct the connectivity using the chosen estimator. We represent these considerations as

$$\widehat{\mathcal{C}}(v, s, t) = f^*(\widehat{f}(f_*(\mathcal{D}(v, s))). \quad (1)$$

142 This makes explicit the data featurization  $f_*$ , statistical estimator  $\widehat{f}$ , and any potential subsequent  
 143 transformation  $f^*$  such as summing over the source and target regions. Denoting  $\mathcal{D}$  as a function of  $v$   
 144 and  $s$  reflects that we consider using different data to estimate connectivities for different cell-classes  
 145 and source regions. Table 1 reviews estimators used for this data-type used in previous work, as well  
 146 as our two main extensions: the Cre-NW and **Expected Loss** (EL) models. Additional information on  
 147 these estimators is given in Supplemental Section ??.

Name	$f^*$	$\hat{f}$	$f_*$	$\mathcal{D}(v, s)$
NNLS (?)	$\hat{f}(1_s)$	NNLS(X,Y)	$X = x_{\mathcal{S}}, Y = y_{\mathcal{T}}$	$I_m/I_m$
NW (?)	$\sum_{l_s \in s} \hat{f}(l_s)$	NW(X,Y)	$X = l_s, Y = y_{\mathcal{T}}$	$I_m/I_m$
Cre-NW	$\sum_{l_s \in s} \hat{f}(l_s)$	NW(X,Y)	$X = l_s, Y = y_{\mathcal{T}}$	$(I_l \cap I_v)/I_m$
Expected Loss (EL)	$\sum_{l_s \in s} \hat{f}(s)$	EL(X, Y, v)	$X = l_s, Y = y_{\mathcal{T}}, v$	$I_l/I_m$

Table 1: Estimation of  $\mathcal{C}$  using connectivity data. The regionalization, estimation, and featurization steps are denoted by  $f^*$ ,  $\hat{f}$ , and  $f_*$ , respectively. The training data used to fit the model is given by index set  $I$ . We denote experiments with centroids in particular major brain divisions and leafs as  $I_m$  and  $I_l$ , respectively. Data  $I_l/I_m$  means that, given a location  $l_s \in s \in m$ , the model  $\hat{f}$  is trained on all of  $I_m$ , but only uses  $I_l$  for prediction. The non-negative least squares estimator (NNLS) fits a linear model that predicts regionalized projection signal  $y_{\mathcal{T}}$  as a function of regionalized injection signal  $x_{\mathcal{S}}$ . Thus, the regionalization step for a region  $s$  is given by applying the learned matrix  $\hat{f}$  to the  $s$ -th indicator vector. In contrast, the Nadaraya-Watson model (NW) is a local smoothing model that generates a prediction for each voxel within the source structure that are then averaged to create estimate the structure-specific connectivity.

148 Our contributions - the Cre-NW and Expected Loss (EL) models - have several differences from the  
 149 previous methods. In contrast to the non-negative least squares (?) and Nadaraya-Watson (?)  
 150 estimators that account only for source region  $s$ , our new estimators account cell class  $v$ . The Cre-NW  
 151 estimator only uses experiments from a particular class to predict connectivity for that class, while the  
 152 EL estimator shares information between classes within a structure. Both of these estimator take into  
 153 account both the cell-class and the centroid position of the experimental injection. Like the NW and  
 154 Cre-NW estimator, the EL estimator generates predictions for each voxel in a structure, and then sums  
 155 them together to get the overall connectivity. However, in contrast to the NW approaches, the EL  
 156 estimate of the projection vector for a cell-class at a location weights the average projection of that  
 157 cell-class in the region containing the location against the relative locations of all experimental  
 158 centroids in the region regardless of class. That is, cell-class and source region combinations with

159 similar average projection vectors will be upweighted when estimating  $\hat{f}$ . Thus, all experiments that  
160 are nearby in three-dimensional space can help generate the prediction, even when there are few  
161 nearby experiments for the cell-class in question. A detailed mathematical description of our new  
162 estimator is given in Supplemental Section ??.

163 ***Model evaluation***

164 We select optimum functions from within and between our estimator classes using **leave-one-out**  
 165 **cross validation**, in which the accuracy of the model is assessed by its ability to predict projection  
 166 vectors experiments excluded from the training data on the basis of their cell class and experimental  
 167 centroid. Equation 1 includes a deterministic step  $f^*$  included without input by the data. The  
 168 performance of  $\hat{\mathcal{C}}(v, s, t)$  is thus determined by performance of  $\hat{f}(f_*(\mathcal{D}(v, s)))$ . Thus, we evaluate  
 169 prediction of  $f_{\mathcal{T}} : \mathbb{R}^3 \rightarrow \mathbb{R}_{\geq 0}^T$  - the regionalized connection strength at a given location.

170 Another question is what combinations of  $v$ ,  $s$ , and  $t$  to generate a prediction for. Our EL and  
 171 Cre-NW models are leaf specific. They only generate predictions for cell-classes in leafs where at least  
 172 one experiment with a Cre-line targeting that class has a centroid. To accurately compare our new  
 173 estimators with less-restrictive models such as used in ?, we restrict our evaluation set to Cre  
 174 driver/leaf combinations that are present at least twice. The sizes of these evaluation sets are given in  
 175 Supplemental Section 5.

We use weighted  $l_2$ -loss to evaluate these predictions.

$$\text{l2-loss } \ell(y_{\mathcal{T}}(i), \widehat{y_{\mathcal{T}}(i)}) := \|y_{\mathcal{T}}(i) - \widehat{y_{\mathcal{T}}(i)}\|_2^2.$$

$$\text{weighted l2-loss } \mathcal{L}(\widehat{f}(f_*)) := \frac{1}{|\{\mathcal{S}, \mathcal{V}\}|} \sum_{s, v \in \{\mathcal{S}, \mathcal{V}\}} \frac{1}{|I_s \cap I_v|} \sum_{i \in (I_s \cap I_v)} \ell(y_{\mathcal{T}}(i), \hat{f}_{\mathcal{T}}(f_*(\mathcal{D}(v, s) \setminus i))).$$

176 This is a somewhat different loss from ?, both because of the normalization of projection, and because  
 177 of the increased weighting of rarer combinations of  $s$  and  $v$  implicit in the  $\frac{1}{|I_s \cap I_v|}$  term in the loss. The  
 178 establishment of a lower limit of detection and the extra cross-validation step used in the EL model to  
 179 establish the relative importance of regionally averaged cell-class projection and injection centroid  
 180 position are covered in Supplemental Section ??.

181 ***Connectivity analyses***

182 We examine latent structure underlying our estimated connectome using two types of unsupervised  
 183 learning. Our use of hierarchical clustering is standard, and so we do not review it here. However, our  
 184 application of non-negative matrix factorization (NMF) to decompose the estimated long-range  
 185 connectivity into **connectivity archetypes** that linearly combine to reproduce the observed  
 186 connectivity of some independent interest. Non-negative matrix factorization refers to a collection of  
 187 **dictionary-learning** algorithms for decomposing a non-negatively-valued matrix such as  $\mathcal{C}$  into  
 188 positively-valued matrices called, by convention, weights  $W \in \mathbb{R}_{\geq 0}^{S \times q}$  and hidden units  $H \in \mathbb{R}_{\geq 0}^{q \times T}$ .  
 189 Unlike PCA, NMF specifically accounts for the fact that data are all in the positive orthant. The matrix  
 190  $H$  is typically used to identify latent structures with interpretable biological meaning, and the choice  
 191 of matrix factorization method reflects particular scientific subquestions and probabilistic  
 192 interpretations.

193 Our algorithm solves the following optimization problem

$$\text{NMF}(\mathcal{C}, \lambda, q) := \arg \min_{W \in \mathbb{R}_{\geq 0}^{S \times q}, H \in \mathbb{R}_{\geq 0}^{q \times T}} \frac{1}{2} \| \mathbf{1}_{d(s,t) > 1500\mu m} \odot \mathcal{C} - WH \|_2^2 + \lambda (\|H\|_1 + \|W\|_1).$$

194 For this decomposition we ignore connections between source and target regions less than  $1500\mu m$   
 195 apart. This is because short-range projections resulting from diffusion dominate the matrices  $\hat{\mathcal{C}}$ , and  
 196 represent a less-interesting type of biological structure. We set  $\lambda = 0.002$  to encourage sparser and  
 197 therefore more interpretable components. We use unsupervised cross-validation to determine an  
 198 optimum  $q$ , and show the top 15 stable components (?). Stability analysis accounts for the  
 199 difficult-to-optimize NMF program by clustering the resultant  $H$  from multiple replicates. Since the  
 200 NMF objective is difficult to optimize and sensitive to initialization, we follow up with a stability  
 201 analysis. The medians of the component clusters appearing frequently across NMF replicates are  
 202 selected as **connectivity archetypes**. Details of these approaches are given in Supplementary Sections  
 203 ?? and ??.

### 3 RESULTS

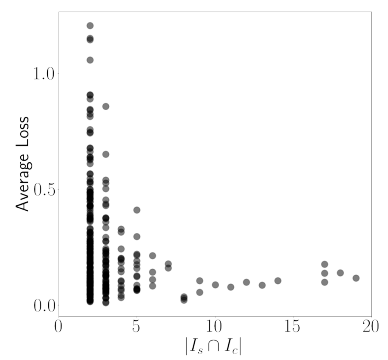
204 We provide several types of results. First, we show that the novel expected-loss (EL) estimator  
 205 performs best in our validation assays. Second, qualitative exploratory analysis confirms that the  
 206 Cre-specific connectivity matrices generated using this model are consistent with known biology.  
 207 Third, statistical decomposition of the wild-type connectivity matrix using unsupervised learning  
 208 shows how archetypal components can combine to produce observed signals.

209 ***Model evaluation***

210 Our EL model generally performs better than the other estimators that we consider. Table 2a contains  
 211 weighted losses from leave-one-out cross-validation of candidate models, such as the NW Major-WT  
 212 model from ?. The EL model combines the good performance of class-specific models like NW  
 213 Leaf-Cre in regions like Isocortex with the good performance of class-agnostic models in regions like  
 214 Thalamus. Additional information on model evaluation, including class and structure specific  
 215 performance, is given in Appendix 5. In particular, Supplementary Table 3 contains the sizes of these  
 216 evaluation sets in each major structure, and Supplementary Section ?? contains the structure- and  
 217 class specific losses.

$\hat{f}_{\mathcal{D}}$	Mean Leaf-Cre Mean $I_c \cap I_L$	NW Major-Cre NW $I_c \cap I_M$	NW Leaf-Cre NW $I_c \cap I_L$	NW Leaf NW $I_L$	NW Major-WT NW $I_{wt} \cap I_M$	NW Major NW $I_M$	EL EL $I_L$
Isocortex	0.239	0.252	0.234	0.279	0.274	0.274	<b>0.228</b>
OLF	0.193	0.233	0.191	<b>0.135</b>	0.179	0.179	0.138
HPF	0.175	0.332	0.170	0.205	0.228	0.228	<b>0.153</b>
CTXsp	<b>0.621</b>	<b>0.621</b>	<b>0.621</b>	<b>0.621</b>	<b>0.621</b>	<b>0.621</b>	<b>0.621</b>
STR	0.131	<b>0.121</b>	0.128	0.169	0.232	0.232	0.124
PAL	0.203	0.205	0.203	0.295	0.291	0.291	<b>0.188</b>
TH	0.673	0.664	0.673	<b>0.358</b>	0.379	0.379	0.369
HY	0.360	0.382	0.353	0.337	0.317	0.317	<b>0.311</b>
MB	0.168	0.191	0.160	0.199	0.202	0.202	<b>0.159</b>
P	0.292	0.292	0.292	0.299	0.299	0.299	<b>0.287</b>
MY	0.268	0.347	0.268	0.190	<b>0.189</b>	<b>0.189</b>	0.204
CB	<b>0.062</b>	<b>0.062</b>	<b>0.062</b>	0.068	0.112	0.112	0.068

(a)



(b)

Table 2: Losses from leave-one-out cross-validation of candidate models. **Bold** numbers are best for their major structure. Empirical performance of selected EL model by data abundance. The model is more accurate in Cre-leaf combinations where it draws on more data.

218 ***Connectivities***

219 Our main result is the estimation of matrices  $\hat{\mathcal{C}}_v \in \mathbb{R}_{\geq 0}^{S \times T}$  representing connections of source structures  
 220 to target structures for particular cre-lines  $v$ . We confirm the detection of several well-established  
 221 connectivities within our tensor, although it is our expectation that additional interesting biological  
 222 processes are also manifest. The connectivity tensor and code to reproduce it are available at  
 223 [https://github.com/AllenInstitute/mouse\\_connectivity\\_models/tree/2020](https://github.com/AllenInstitute/mouse_connectivity_models/tree/2020).

224 *Overall connectivity* Several expected biological projection patterns are evident in the wild-type  
 225 connectivity matrix  $\mathcal{C}_{wt}$  from leaf sources to leaf targets shown in Figure 2a. Intraareal connectivities  
 226 are clear, as are ipsilateral connections between cortex and thalamus. The clear intrastructural and  
 227 intraareal connectivities mirror previous estimates in ? and ? and descriptive depictions of individual  
 228 experiments in ?.

229 Our estimated wild-type connectivities appear more variable than those in ?, which used the NW  
 230 Major-WT model whose accuracy is evaluated in Table 2a. This is plausibly because of both the  
 231 layer-specific targeting of the different cre-lines, and also the layer-specificity of the selected model.  
 232 Although layer-specificity is a major advantage of including distinct cre-lines, for comparison, we also  
 233 plot coarser projections between summary-structure sources and targets in the cortex in Figure 2b.  
 234 These are averages over component layers weighted by layer size. These connectivities exhibit a finer  
 235 differentiation between regions and lower limit of detection than those in ?, and are grossly congruent  
 236 with prior work. Importantly, as shown in Table 2a this finer spatial resolution corresponds to the  
 237 increased accuracy of our EL model over the NW Major-WT model.

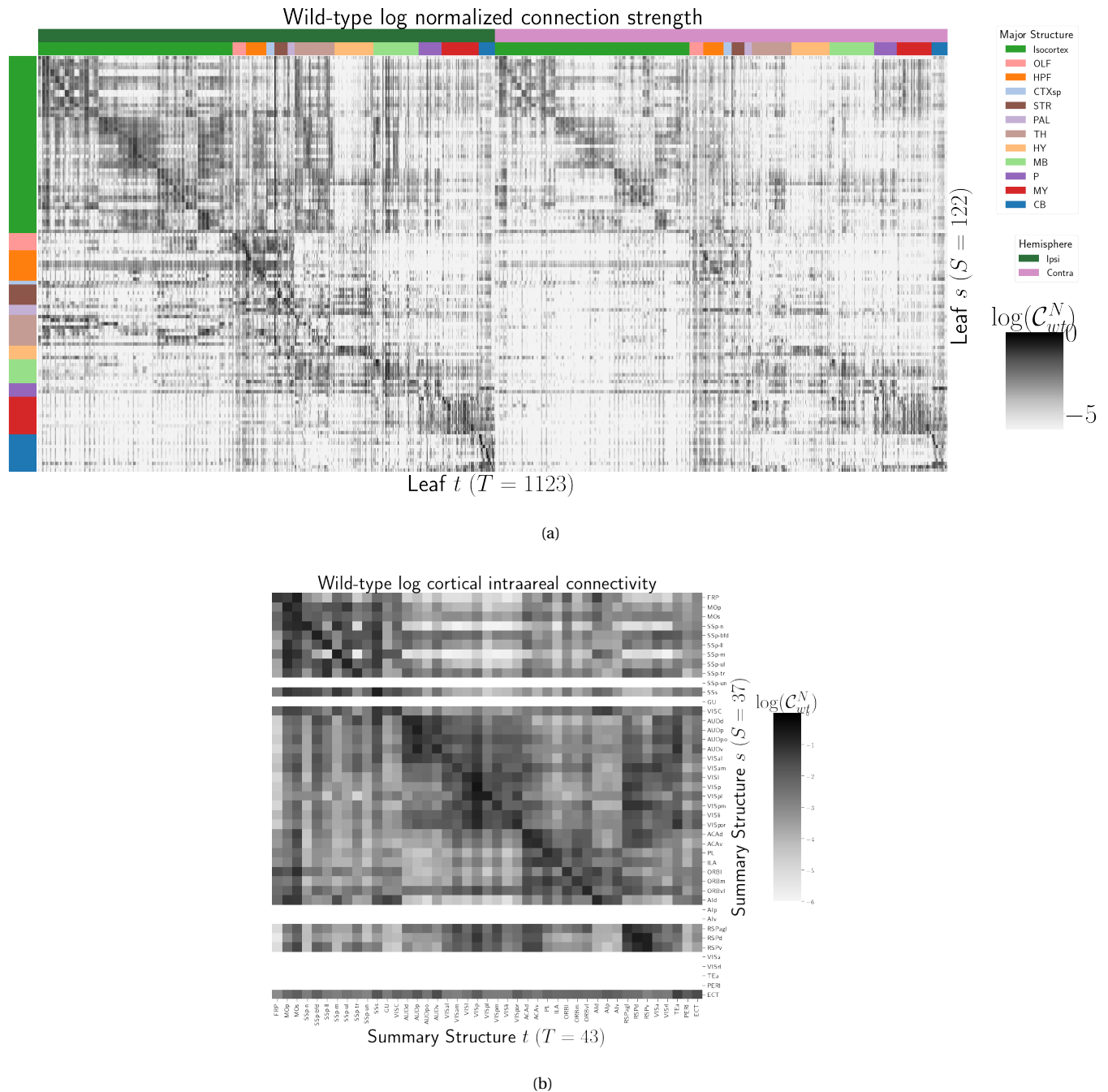


Figure 2: Wild-type connectivities. 2a Log wild-type connectivity matrix  $\log \mathcal{C}(s, t, v_{wt})$ . 2b Log wild-type intracortical connectivity matrix at the summary structure level.

238 *Class-specific connectivities* Source and cell-type combinations which project similarly indicate the  
 239 network structure underpinning cognition. Although there is a rich anatomical literature using  
 240 anterograde tracing data to describe projection patterns from subcortical sources to a small set of  
 241 targets of interest, most accessible whole brain projection data are from the Allen Mouse Connectivity  
 242 Atlas (MCA) project used here to generate the connectome models. Thus, to validate our results while  
 243 avoiding a circular validation of the data used to generate the model weights, we confirm that these  
 244 class-specific connectivities exhibit certain known behaviors. In particular, we focus on several cell  
 245 types and source areas with extensive previous anatomical descriptions of projections using both bulk  
 246 tracer methods with cell type specificity and single cell reconstructions: 1) thalamic-projecting  
 247 neurons in the visual and motor cortical regions, 2) cholinergic neurons in the medial septum and  
 248 nucleus of the diagonal band (MS/NDB); 3) cholinergic neurons in the caudoputamen, and 4)  
 249 serotonergic neurons of the dorsal raphe nucleus (DR). We find that our inferred connections are in  
 250 agreement with literature on these cell types.

251 DEPENDENCE OF THALAMIC CONNECTION ON CORTICAL LAYER. Visual cortical areas VISp and VISl and  
 252 cortical motor areas MOp and MOs are ideal testbeds for our connectivities because there are  
 253 well-established layer-specific projection patterns that can be labeled with the layer-specific cre-lines  
 254 from the Allen datasets and others ??, and are also well-represented in our dataset. Figure 3a shows  
 255 that in VISp, the Ntsr1-Cre line strongly targets the core part of the thalamic LGd nucleus while in VISl  
 256 has a very strong projection to the LP nucleus. In VISp, the Rbp4-Cre strongly targets LP as well.  
 257 Recall that we display connectivity estimates for structures with at least one injection centroid in the  
 258 structure. Thus, the position of non-zero rows in Figure 3a shows the localization of Rbp4-Cre and  
 259 Ntsr1-Cre injection centroids to layers 5 and 6 respectively. This is further examined in Supplemental  
 260 Section ??). Thus, as a heuristic alternative model, to also synthesize information about leafs targeted  
 261 by different cre-lines, we also display an average connectivity matrix over all cre-lines. This combined  
 262 output is not evaluated in our testing, and is only a general stand-in for overall behavior, but provides  
 263 a useful summary of results.

264 MS AND NDB PROJECTIONS IN THE CHAT-IRES-CRE-NEO MODEL. Cholinergic neurons in the MS and  
 265 NDB are well-known to strongly innervate the hippocampus, olfactory bulb, piriform cortex,  
 266 entorhinal cortex, and lateral hypothalamus (??). In the Allen MCA, cholinergic neurons were labeled

267 by injections into Chat-IRES-Cre-neo mice. We first checked the estimated connectome weights to  
 268 targets in these major brain divisions from MS and NDB. We observed that all these expected divisions  
 269 were represented above the 90th percentile of weights. Recently, a single cell whole brain mapping  
 270 project using Chat-Cre mice fully reconstructed n=50 cells, revealing these same major targets and  
 271 also naming additional targets from MS/NDB (?). We compared our Chat-IRES-Cre connectome  
 272 model data for MS and NDB with the targets identified by ?. We identified 150 targets at the fine leaf  
 273 structure level in the top 10% of estimated weights. To directly compare our data across studies, we  
 274 had to merge structures as needed to get to the same ontology level and remove ipsilateral and  
 275 contralateral information. After formatting our data, we found 51 targets in the top 10%; Li et al.  
 276 reported 47 targets across the 50 cells. There was good consistency overall between the target sets; 35  
 277 targets were shared, 12 were unique to the single cell dataset, and 16 unique to our model data. We  
 278 checked whether targets missing from our dataset were because of the threshold level. Indeed,  
 279 lowering the threshold to the 75 th percentile confirmed 6 more targets-in-common, and all but 2  
 280 targets from ? were above the 50th percentile weights in our model. Of note, the absence of a target in  
 281 the single cell dataset that was identified in our model data is most likely due to the sparse sampling  
 282 of all possible projections from only n=50 MS/NDB cells.

283 CP PROJECTIONS IN THE CHAT-IRES-CRE-NEO MODEL. Most cells in the caudoputamen (CP) are  
 284 GABAergic spiny projection neurons. These cells are also the only type that send projections outside  
 285 the CP. Cholinergic interneurons make up 1-2% of all CP cells and their axon terminals do not extend  
 286 beyond the CP borders. We confirmed that the model predictions for connection weights from CP  
 287 cholinergic cells were consistent with this known anatomy; the connection weight to CP was ~ 2-fold  
 288 higher than any other in the top 5%.

289 DR PROJECTIONS IN THE SLC6A4-CRE'ET33 MODEL. Serotonergic projections from cells in the  
 290 dorsal raphe (DR) are widely distributed and innervate many forebrain structures including isocortex  
 291 and amygdala. In the Allen MCA, serotonergic neurons were labeled using Slc6a4-Cre\_ET33 and  
 292 Slc6a4-CreERT2\_EZ13 mice. This small nucleus appears to contain a complex mix of molecularly  
 293 distinct serotonergic neuron subtypes with some hints of subtype-specific projection patterns (???).  
 294 We expect that the Cre lines we used here in the Allen MCA, which utilize the serotonin transporter  
 295 promoter (Slc6a4-Cre and -CreERT2), will lead to expression of tracer in all the serotonergic subtypes

296 recently described in an unbiased way, but this assumption has not been tested directly. We  
297 compared our model data to a single cell reconstruction dataset consisting of n=50 serotonergic cells  
298 with somas in the DR that also had bulk tracer validation ([SK's comment:INSERT LINK TO FIGURE](#)). ?  
299 listed 55 targets across the single cell reconstructions. After processing our data to match the target  
300 structure ontology level across studies, we identified 37 targets from the DR with weights above the 90  
301 th percentile; 27 of these targets matched those named by ?. Overall there was good consistency  
302 between targets in olfactory areas, cortical subplate, CP, ACB and amygdala areas, as well in pallidum  
303 and midbrain.

304 The two major brain divisions with the least number of matches are the isocortex and thalamus.  
305 There are a few likely reasons for these observations. First, in the isocortex, there is known to be  
306 significant variation in the density of projections across different locations, with the strongest  
307 innervation in lateral and frontal orbital cortices ???. Indeed, when we lower the threshold and check  
308 for weights of the targets outside of the 90%, we see all but one of these regions (PTLp, parietal cortex  
309 which is not frontal or lateral) has a weight assigned in the top half of all targets. In the thalamus, it  
310 was also interesting to observe that our model predicted strong connections to several medial  
311 thalamic nuclei (i.e., MD, SMT), that were not targeted by the single cells. This discrepancy may be at  
312 least partially explained by the complex topographical organization of the DR that, like the molecular  
313 subtypes, is not yet completely understood. A previous bulk tracer study that specifically targeted  
314 injections to the central, lateral wings, and dorsal subregions of the DR reported semi-quantitative  
315 differences in projection patterns (?). Notably, ? report that cells in the ventral region of DR project  
316 more strongly to medial thalamic nuclei, whereas the lateral and dorsal DR cells innervate more lateral  
317 regions (e.g., LGd). So it is possible that the single cell somas did not adequately sample the entire DR.

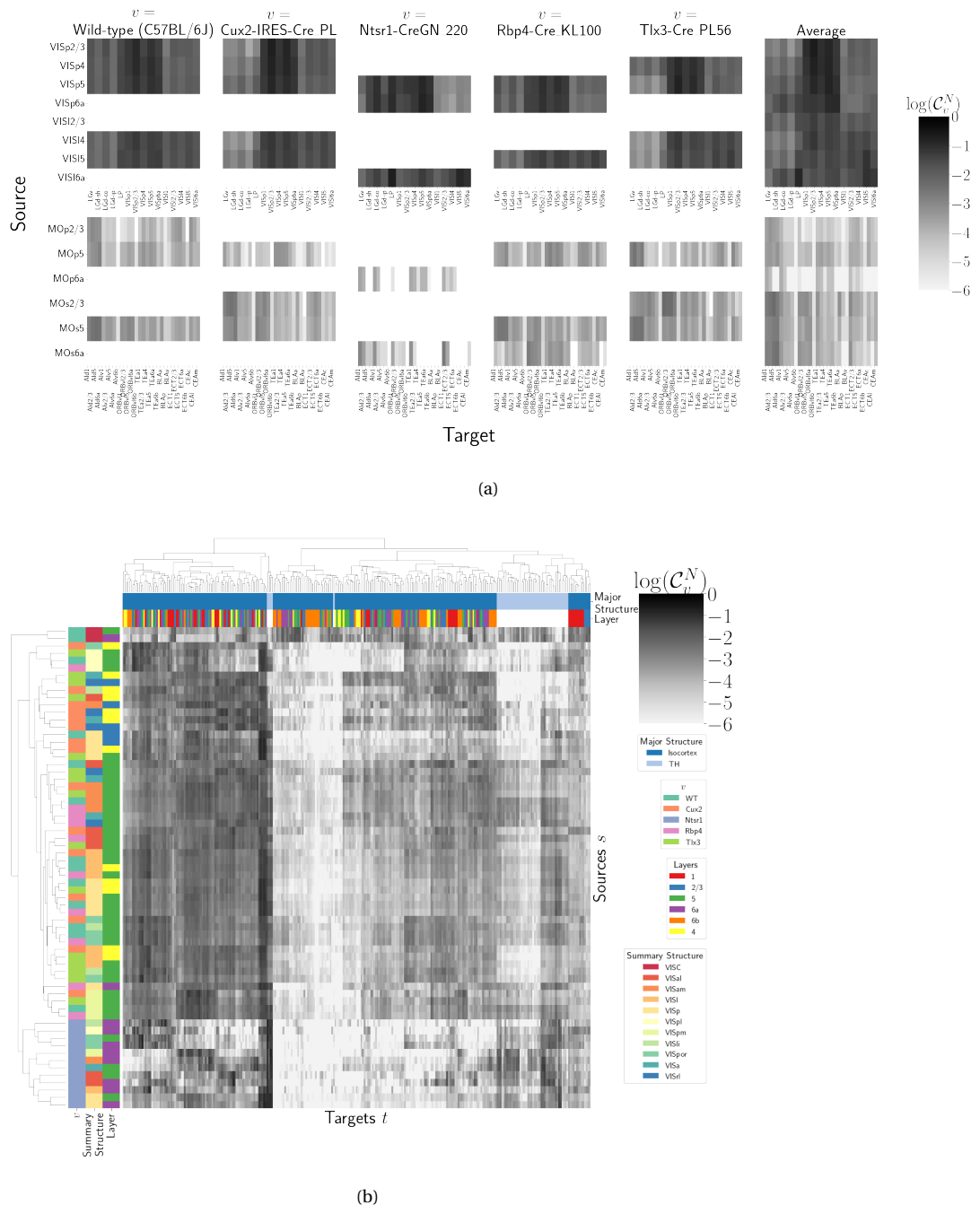


Figure 3: Cell-class specificity. 3a Selected cell-class and layer specific connectivities from two visual and two motor areas. Sources without an injection in the Cre driver line are not estimated due to lack of data for that Cre-line in that structure. 3b Hierarchical clustering of connectivity strengths from visual cortex cell-types to cortical and thalamic targets. Cre-line, summary structure, and layer are labelled on the sources. Major brain division and layer are labelled on the targets.

**318 Connectivity Analyses**

319 Cell-class, while often correlated with cortical layer, can be a stronger driver of connectivity than  
 320 summary structure especially when looking at targets at major brain division level. Figure 3b shows a  
 321 collection of connectivity strengths generated using cre-specific models for wild-type, Cux2, Ntsr1,  
 322 Rbp4, and Tlx3 cre-lines from VIS areas at leaf level in the cortex to cortical and thalamic nuclei. We  
 323 use hierarchical clustering to sort source structure/cell-class combinations by the similarity of their  
 324 structural projections, and sort target structures by the structures from which they receive projections.  
 325 Examining the former, we can see that the layer 6 Ntsr1 Cre-line distinctly projects to thalamic nuclei,  
 326 regardless of source summary structure. This contrasts with the tendency of other cell-classes to  
 327 project intracortically in a manner determined by the source structure. Similarly, layer 6 targets are  
 328 not strongly projected to by any of the displayed cell classes. There are too many targeted summary  
 329 structures to plot here, but we expect that the source profile of each target clusters by structure.

330 In this section, we apply non-negative matrix factorization to decompose the long-range wild-type  
 331 connectivities into linear combinations of archetypal connectivities. This decomposes the remaining  
 332 censored connectivity matrix into a linear model based off a relatively small number of distinct  
 333 signals. This model is able to capture a large amount of the observed variability, and recovers  
 334 structure-specific archetypal signals.

335 These signals are plotted in Figure 4, and technical details and intermediate results are given in  
 336 Supplemental Sections ?? and ??, respectively. These details include a cross-validation based method  
 337 for selecting the number of components, a masking method for focusing only on long range  
 338 connections, and a stability method for ensuring that the decomposition is reliable across  
 339 computational replicates. The plotted decomposition shows that these underlying connectivity  
 340 archetypes correspond strongly to major brain division in both target and sources.

341 Inspection of the reconstructed distal normalized connection strength using the top 15  
 342 components shows qualitatively shows that this relatively sparse decomposition is able to capture  
 343 much of the observed variability. Other connectivity patterns like cortical-cortical and  
 344 cortical-thalamic are also detected.

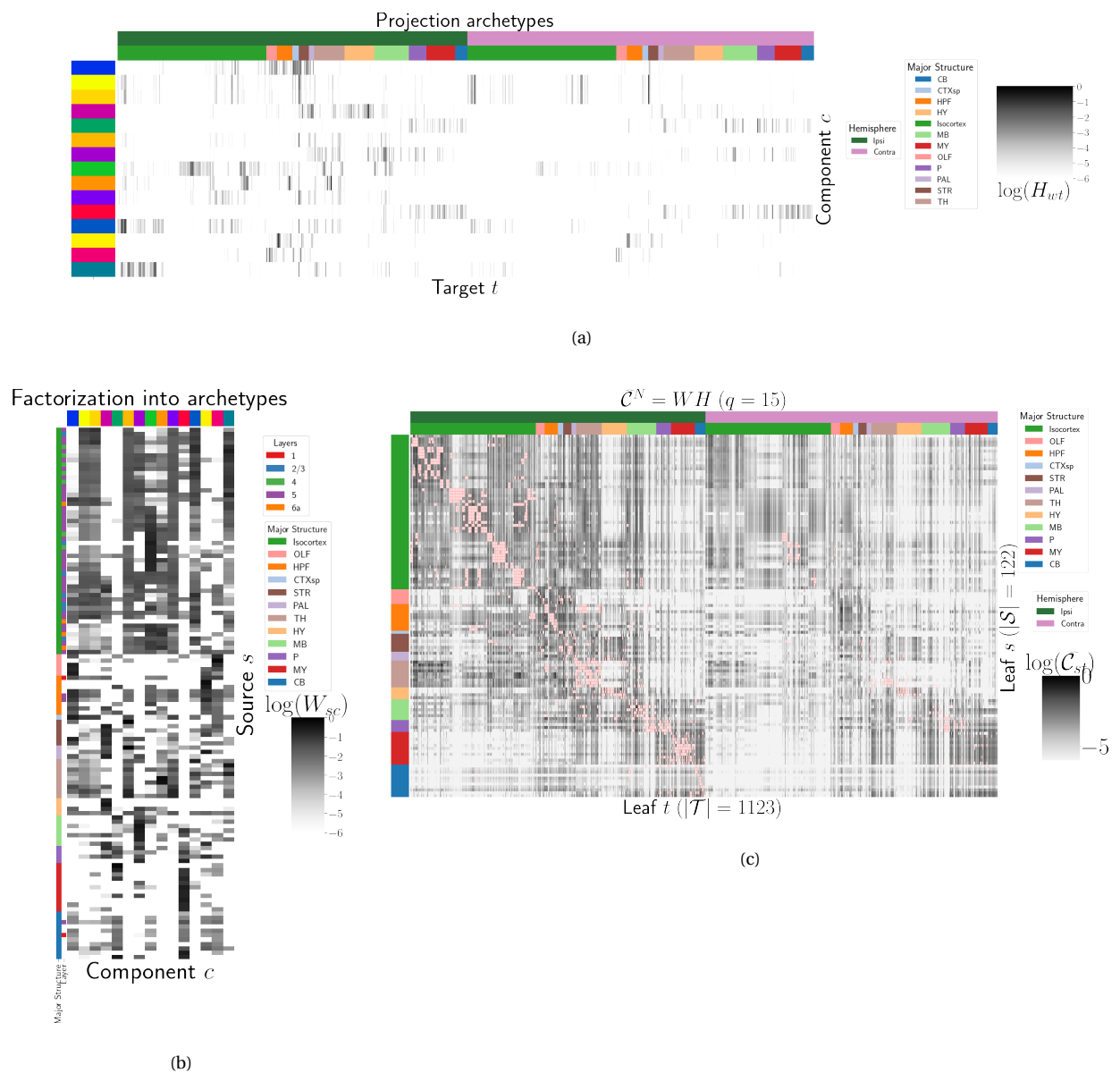


Figure 4: Non-negative matrix factorization results  $\mathcal{C}_w^N = W H$  for  $q = 15$  components. 4a Latent space coordinates  $H$  of  $\mathcal{C}$ . Target major structure and hemisphere are plotted. 4b Loading matrix  $W$ . Source major structure and layer are plotted. 4c Reconstruction of the normalized distal connectivity strength using the top 15 archetypes. Areas less than  $1500 \mu\text{m}$  apart are not modeled, and therefore shown in red.

## 4 DISCUSSION

345 The model presented here is the first cell-type specific whole brain projectome model for a  
 346 mammalian species, and it opens the door for a large number of models linking brain structure to  
 347 computational architectures. Overall, we find expected targets, based on our anatomical expertise  
 348 and published reports, but underscore that the core utility of this bulk connectivity analysis is not  
 349 only in validation of existing connection patterns, but also in identification of new ones. We note that  
 350 although the concordance appeared stronger for the cholinergic cells than the serotonergic cells, any  
 351 differences might still be explained by the lack of high quality “ground-truth” datasets to validate  
 352 these Cre connectome models. Larger numbers of single cell reconstructions, that saturate all  
 353 possible projection types, would be a better gold standard than the small number of cells reported  
 354 here (n=50 for each). ([SK's comment: add citation](#)) Perhaps future iterations of the connectome model  
 355 may also take into account some single cell axon projection data.

356 The Nadaraya-Watson estimator presented here is novel. Beyond using a Nadaraya-Watson kernel  
 357 regression defined in physical space, we define a cell-type space based on similarities of projections,  
 358 and theoretically justify the use of an intermediate shape-constrained estimator. While methods like  
 359 non-negative least squares can also account for covariates, the centroid method from ? was shown  
 360 that the more precise notion of injection location than the non-negative least squares in ?.  
 361 Furthermore, our sample size seems too low to utilize a fixed or mixed effect, particularly since the  
 362 impact of the virus depend on the particular injection region. In a sense both the NNLS and NW  
 363 models can be thought of as improvements over the structure-specific average, and so is also possible  
 364 that a yet undeveloped residual-based data-driven blend of these models could provide improved  
 365 performance.

366 We see several other opportunities for improving on our model. Ours is certainly not the first  
 367 cross-validation based model averaging method ?. However, our use of shape-constrained estimator  
 368 in target-encoded feature space is novel and fundamentally different from Nadaraya-Watson  
 369 estimators that use an optimization method for selecting the weights (?). The properties of this  
 370 estimator, as well as its relation to estimators fit using an optimization algorithm, are a possible future  
 371 avenue of research. A deep model such as ? could be appropriate, provided enough data was  
 372 available. Finally, a Wasserstein-based measure of injection similarity per structure would combine

<sup>373</sup> both the physical simplicity of the centroid model while also incorporating the full distribution of the  
<sup>374</sup> injection signal.

<sup>375</sup> The factorization of the connectivity matrix could also be improved and better used. From a  
<sup>376</sup> statistical perspective, stability-based method for establishing archetypal connectivities in NMF is  
<sup>377</sup> similar to those applied to genomic data ?? . However, non-linear data transformations or matrix  
<sup>378</sup> decompositions, or tensor factorizations that account for correlations between cell-types could better  
<sup>379</sup> capture the true nature of archetypal neural connections. It would also be of great interest to associate  
<sup>380</sup> the archetypal signals detected from connectivity analysis with undergirding gene expression patterns  
<sup>381</sup> or functional information.

<sup>382</sup> Inspired by how this complexity arises from a relatively parsimonious set of genetic information  
<sup>383</sup> during development, w Such components can provide a link to the genetic origin of the regionalized  
<sup>384</sup> connectivity.

## ACKNOWLEDGMENTS

<sup>385</sup> We thank the Allen Institute for Brain Science founder, Paul G. Allen, for his vision, encouragement,  
<sup>386</sup> and support.

387 This supplement is divided into information about our dataset, supplemental methods, and  
388 supplemental results. However, certain topics are revisited between sections. Thus, if a reader is  
389 interested in, say, non-negative matrix factorization, they may find relevant information in both  
390 methods and results.

## 5 SUPPLEMENTAL INFORMATION

391 Our supplementary information consists of abundances of leaf/Cre-line combinations, information  
392 about distances between structures, and the size of our restricted evaluation dataset.

### 393 *Cre/structure combinations in $\mathcal{D}$*

394 This section describes the abundances of leaf and Cre-line combinations in our dataset. Users of the  
395 connectivity matrices who are interested in a particular Cre-line or structure can see the quantity and  
396 type of data used to compute and evaluate that connectivity.

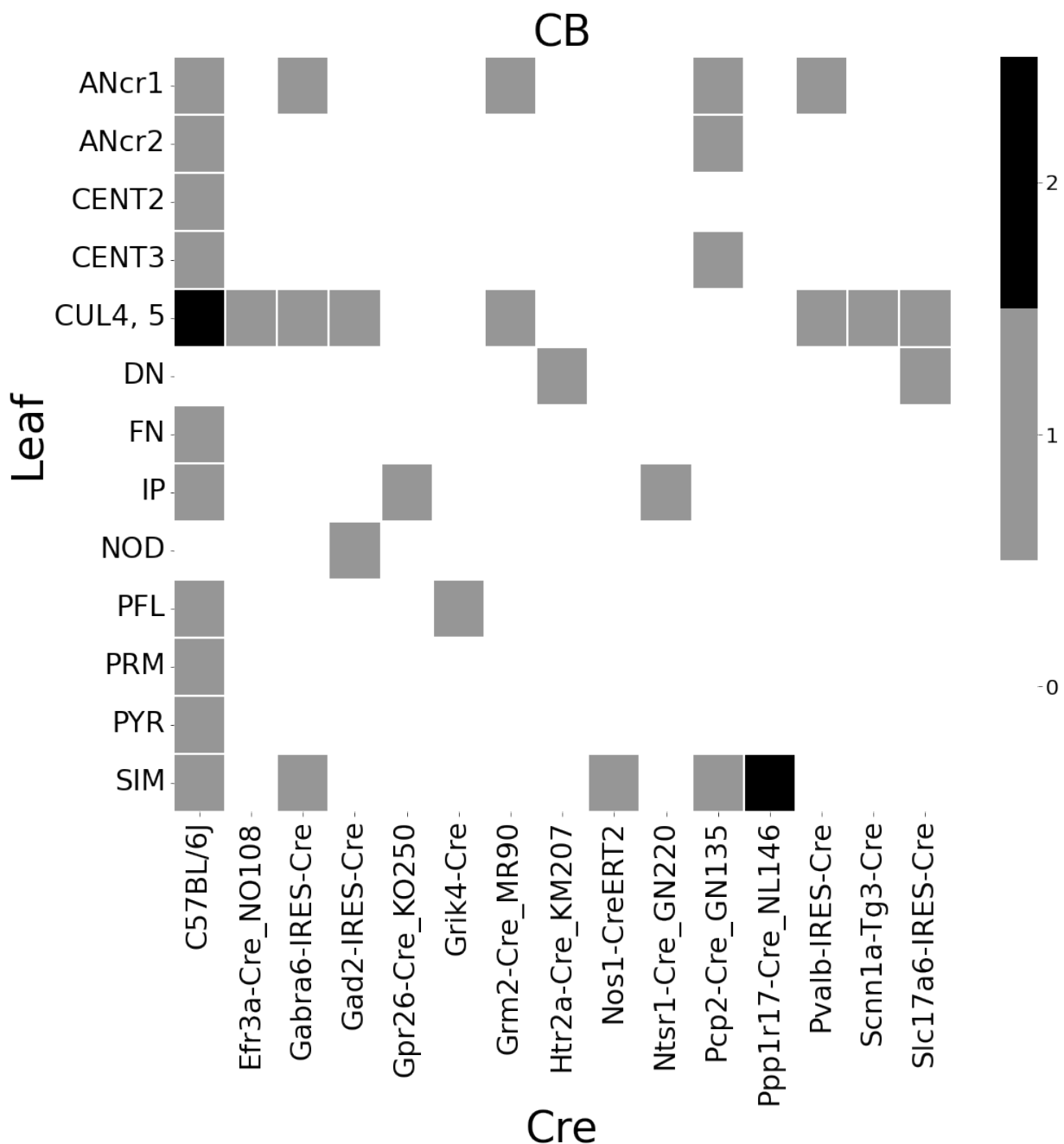


Figure 5: Abundances of Cre-line and leaf-centroid combinations.

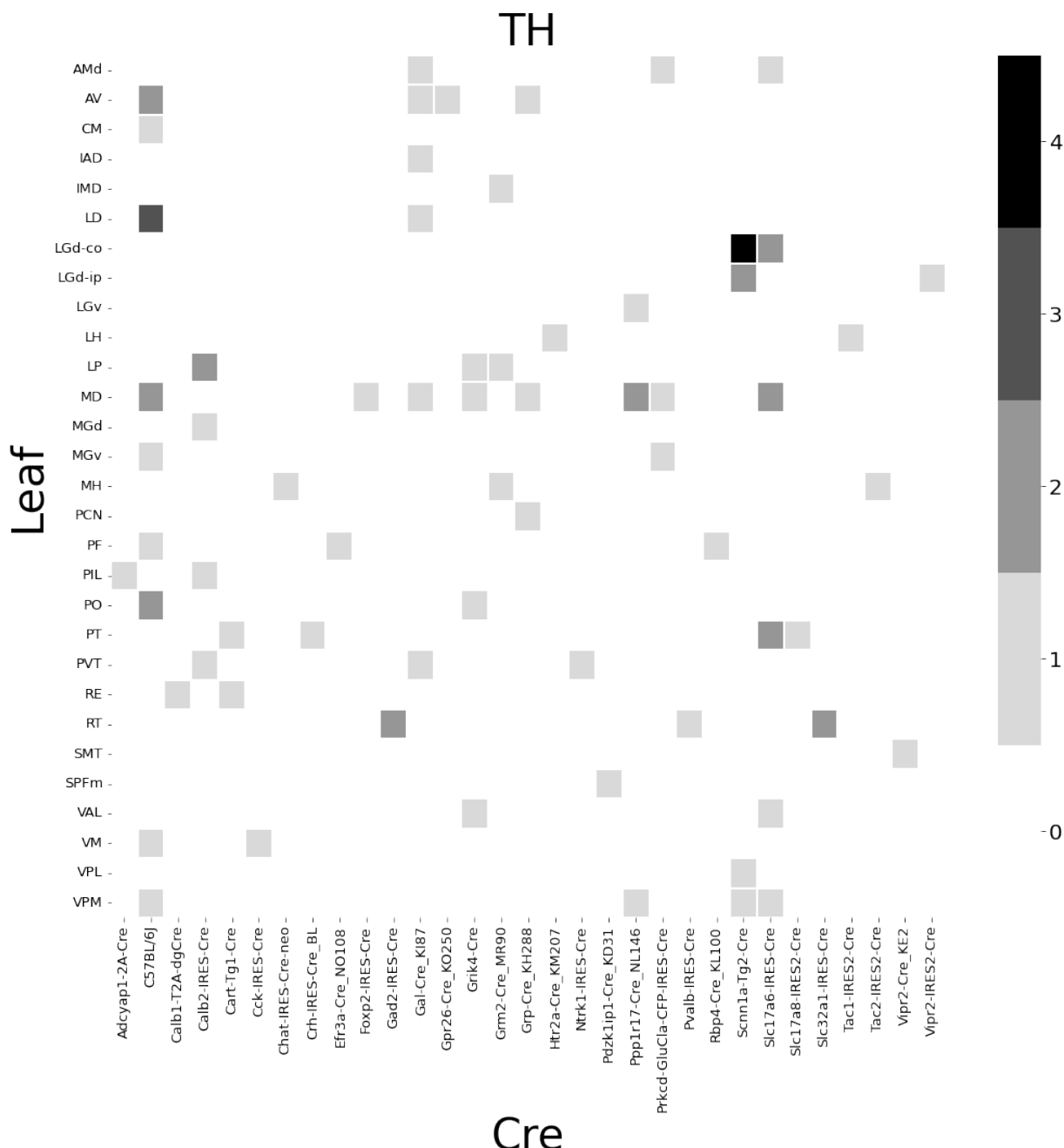


Figure 6: Abundances of Cre-line and leaf-centroid combinations.

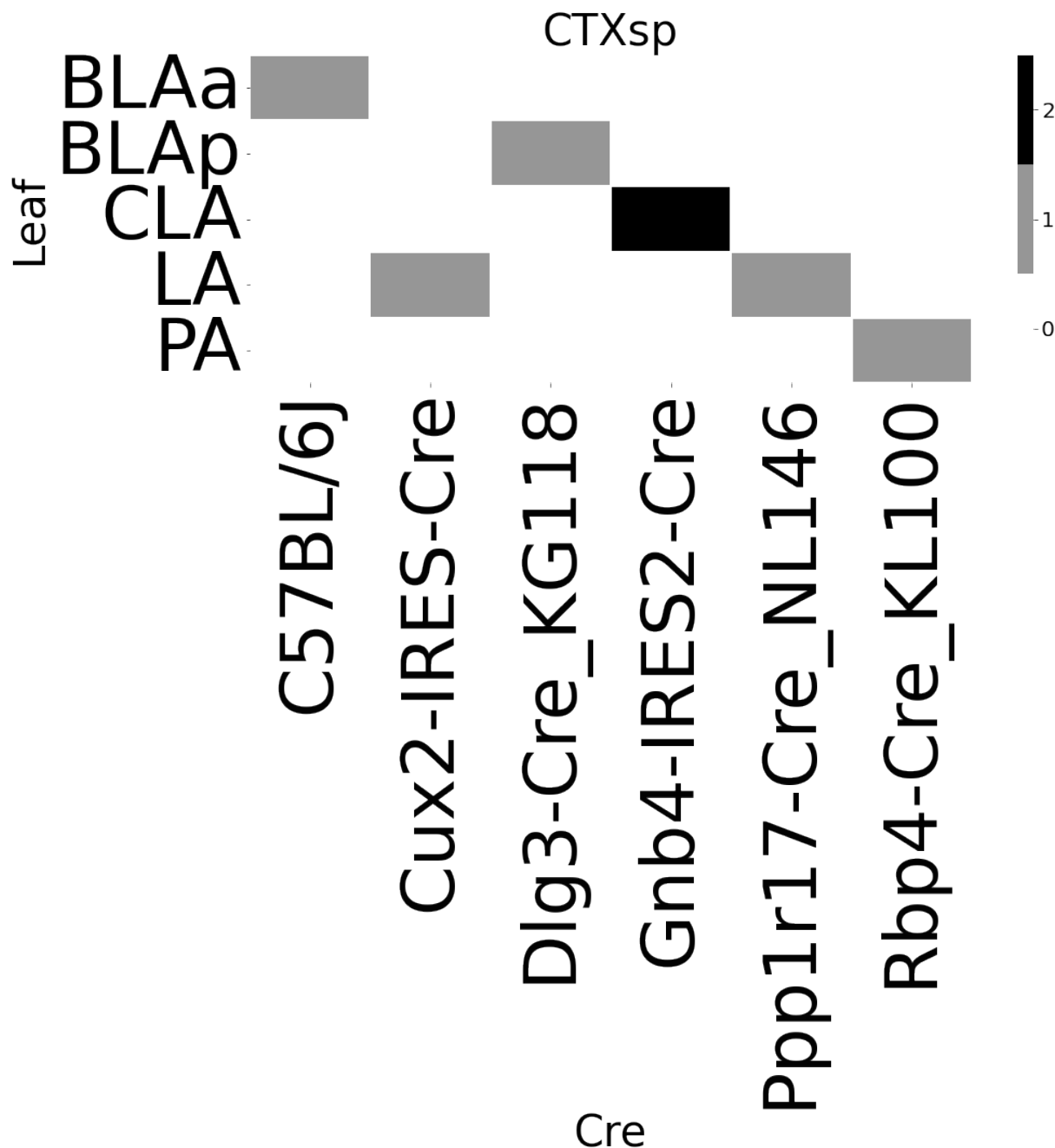


Figure 7: Abundances of Cre-line and leaf-centroid combinations.

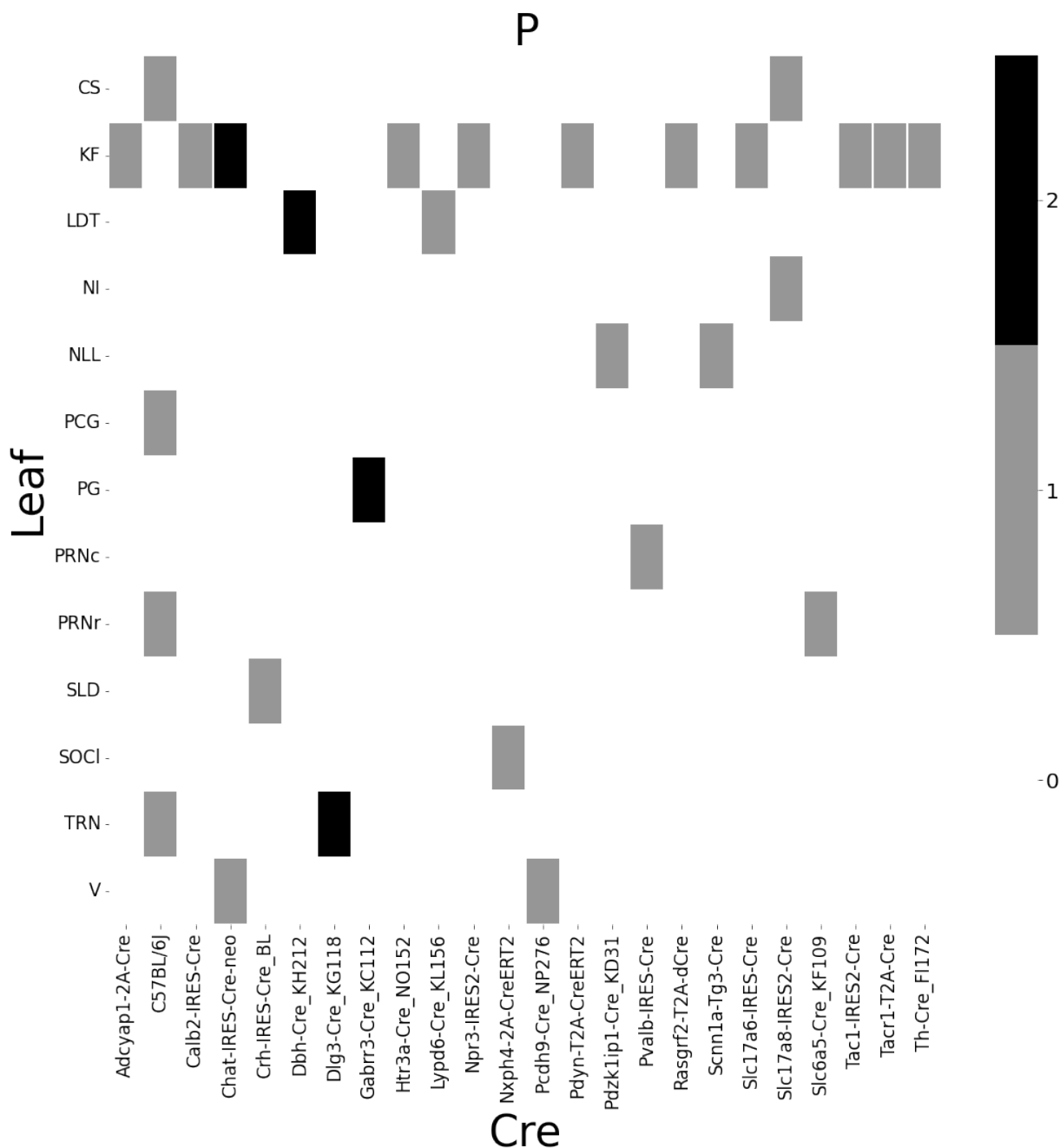


Figure 8: Abundances of cre-line and leaf-centroid combinations.

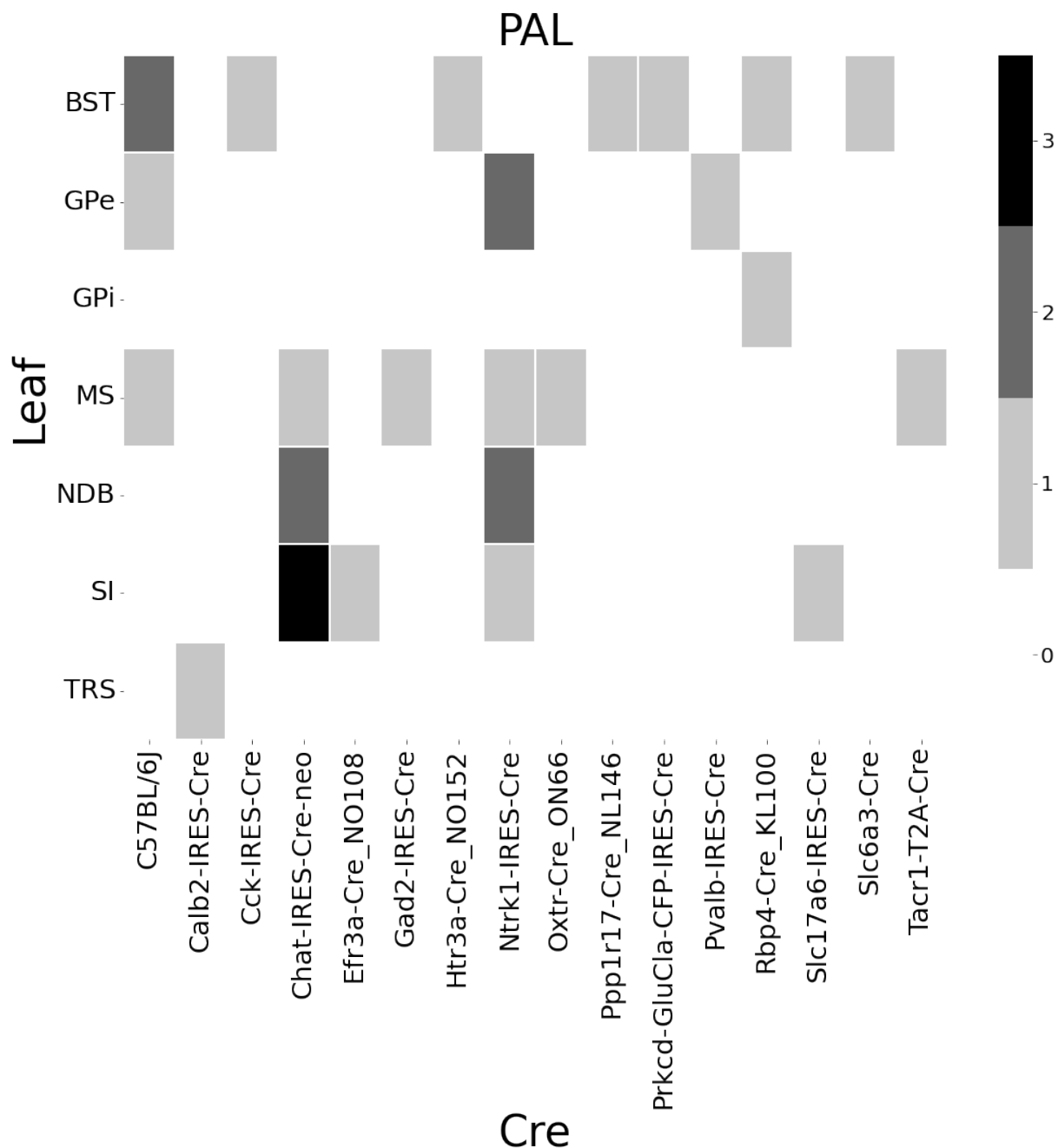


Figure 9: Abundances of Cre-line and leaf-centroid combinations.

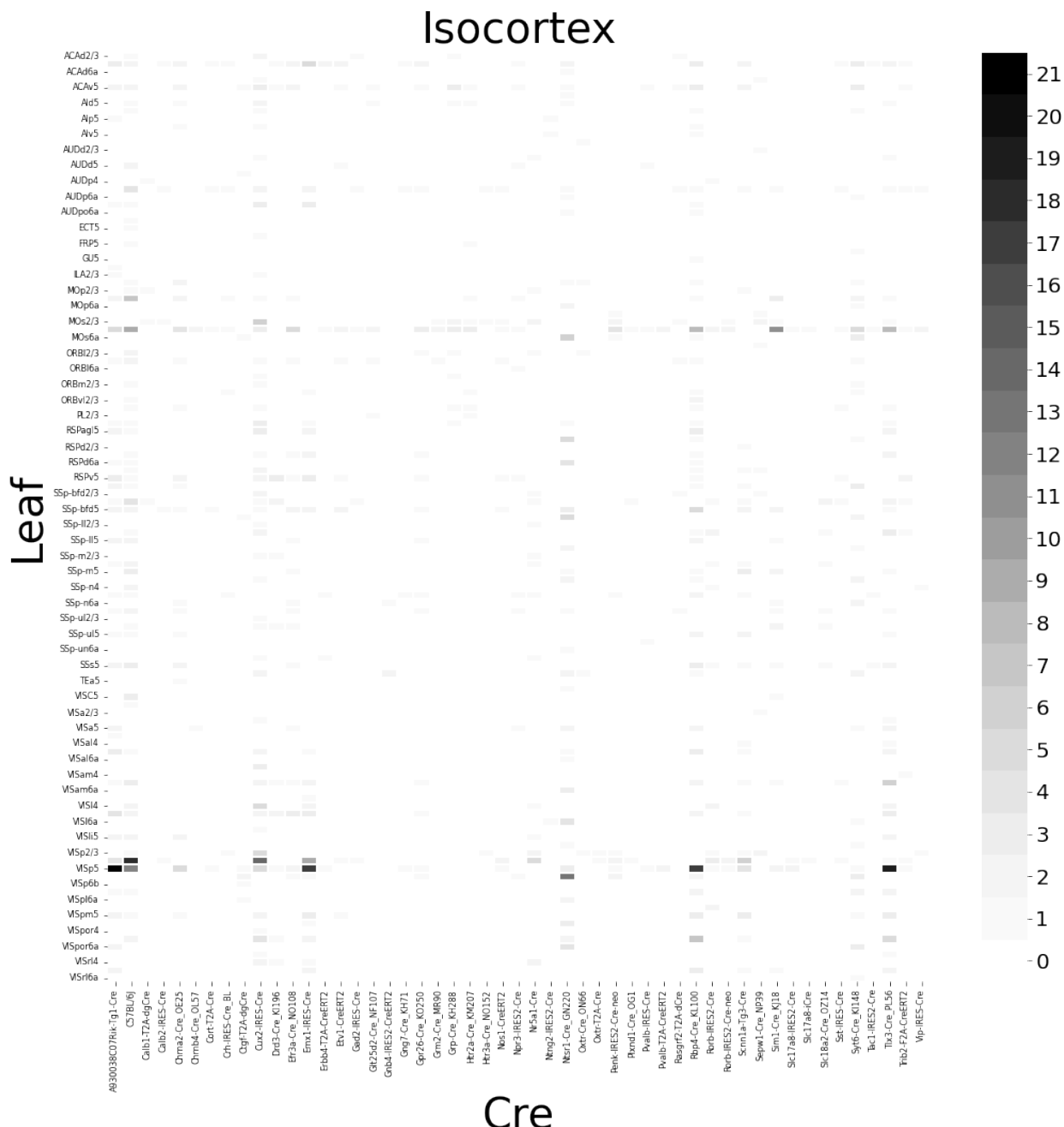


Figure 10: Abundances of Cre-line and leaf-centroid combinations.

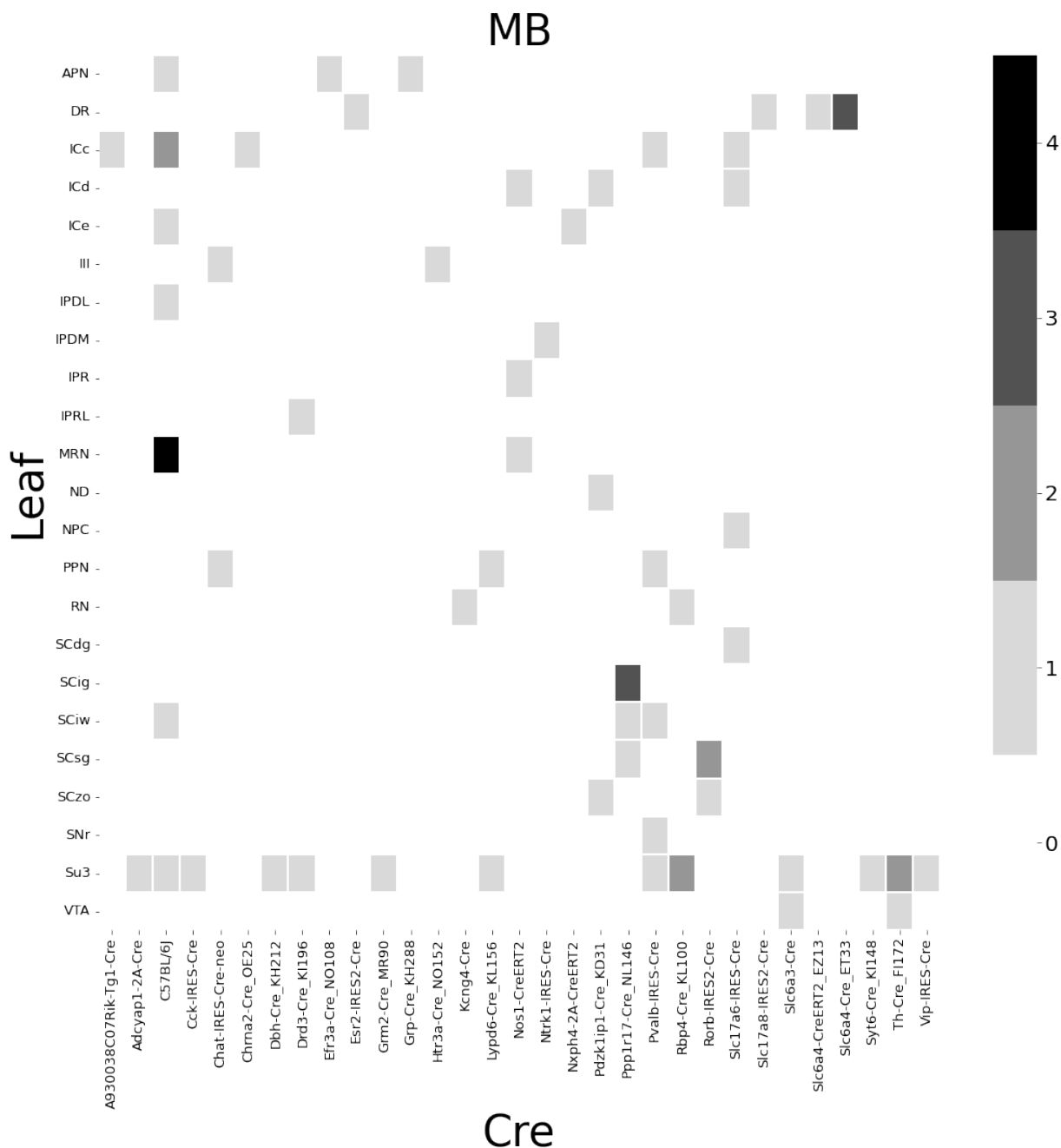


Figure 11: Abundances of Cre-line and leaf-centroid combinations.

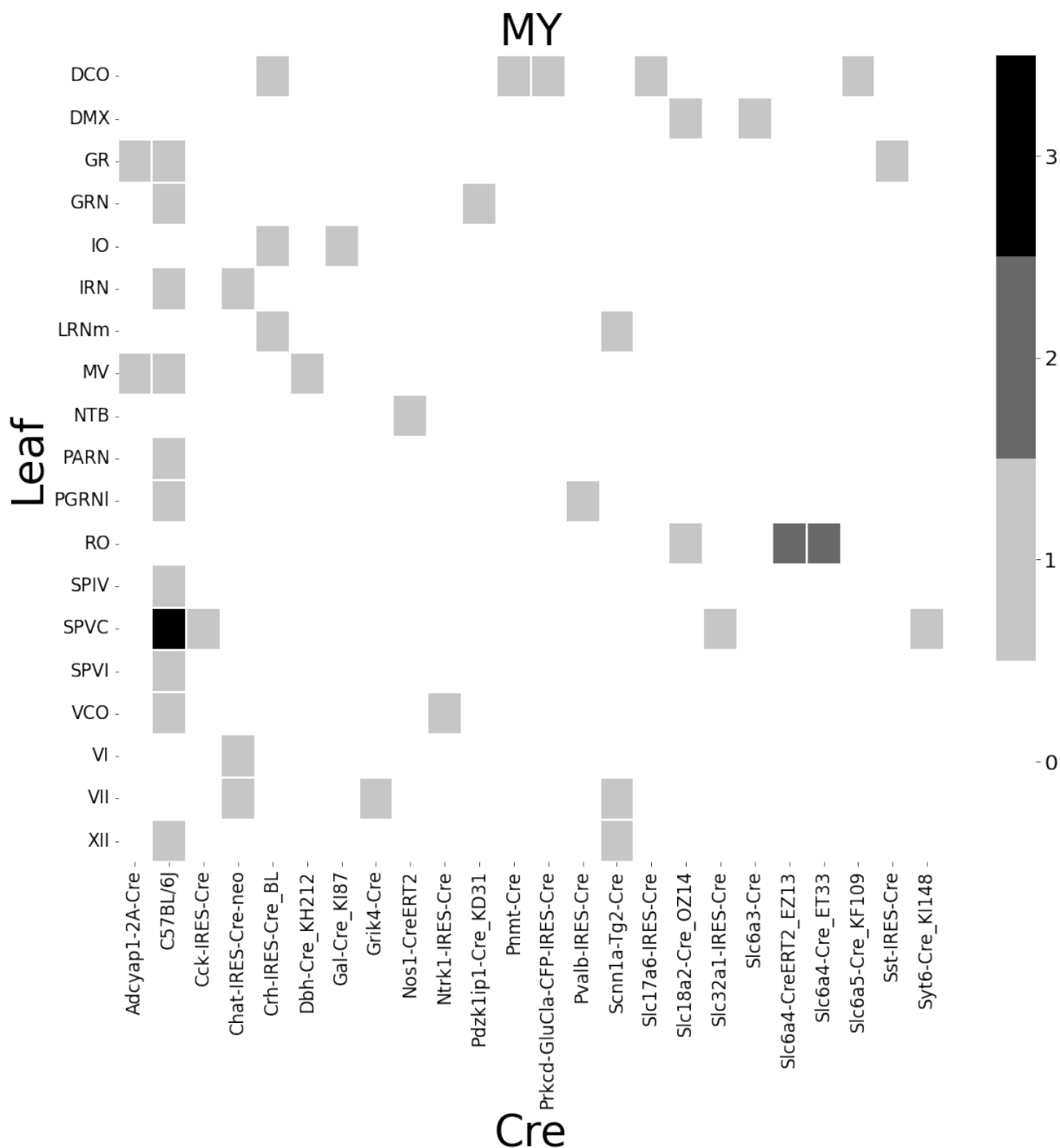


Figure 12: Abundances of Cre-line and leaf-centroid combinations.

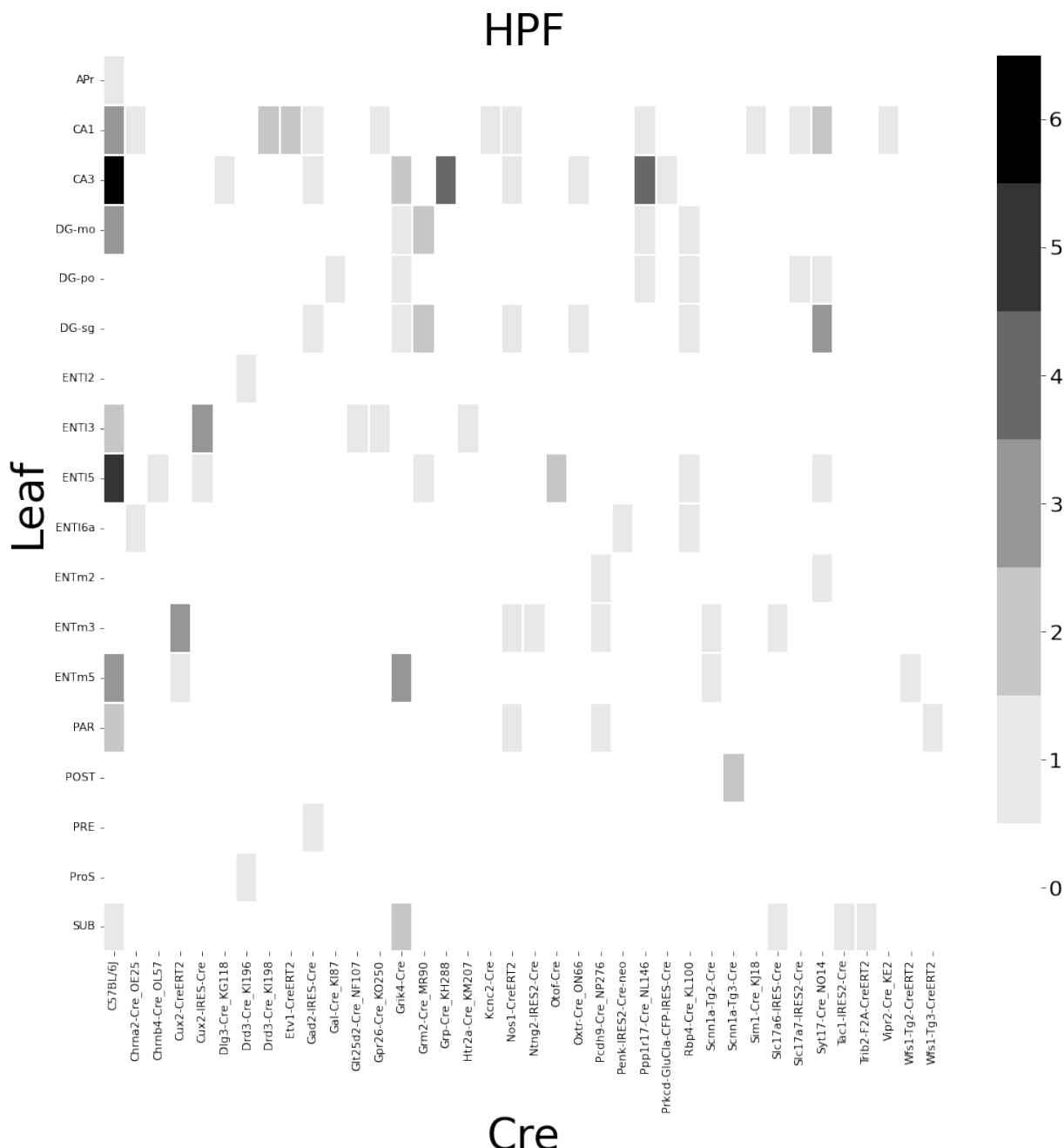


Figure 13: Abundances of Cre-line and leaf-centroid combinations.

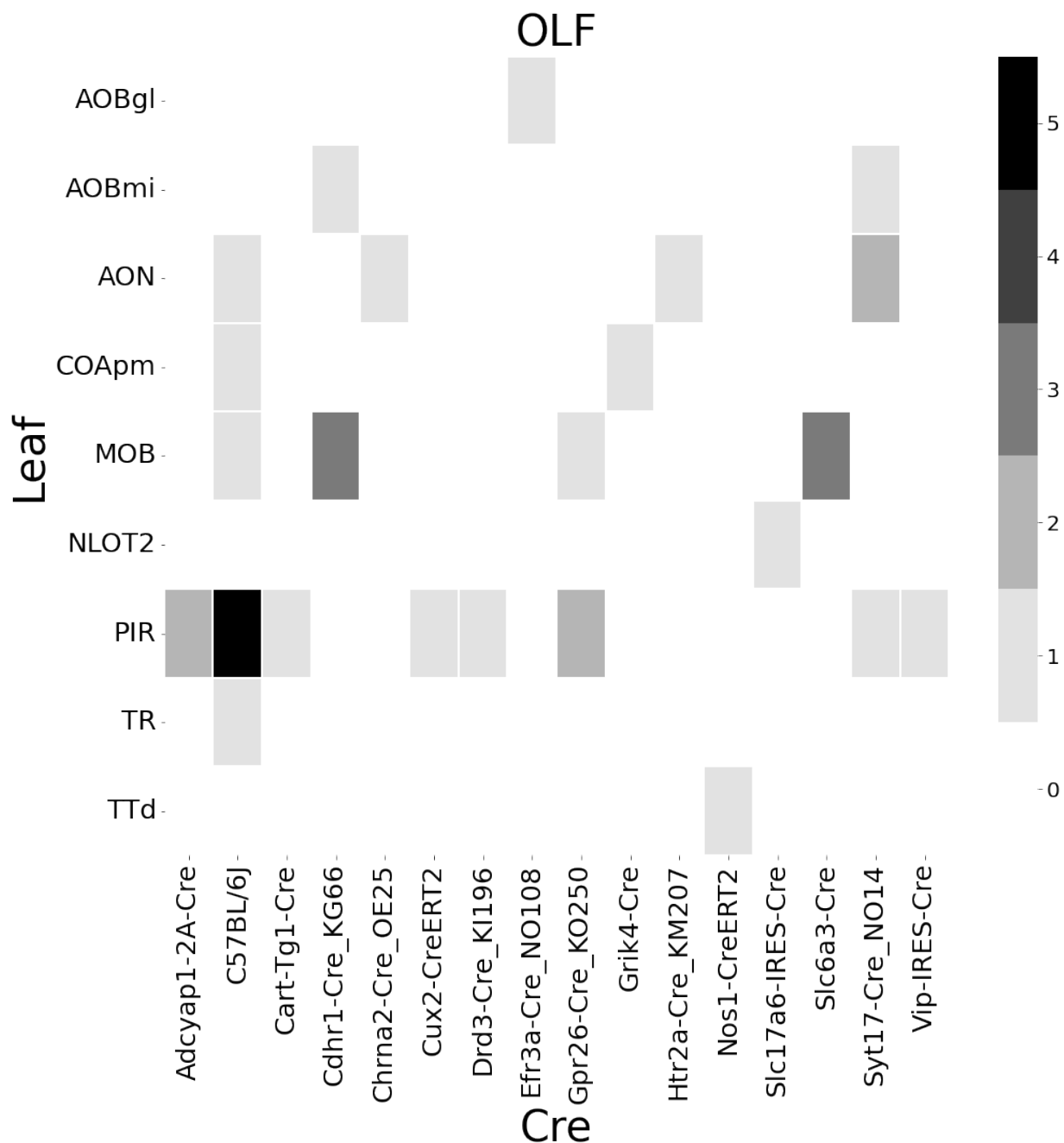


Figure 14: Abundances of Cre-line and leaf-centroid combinations.

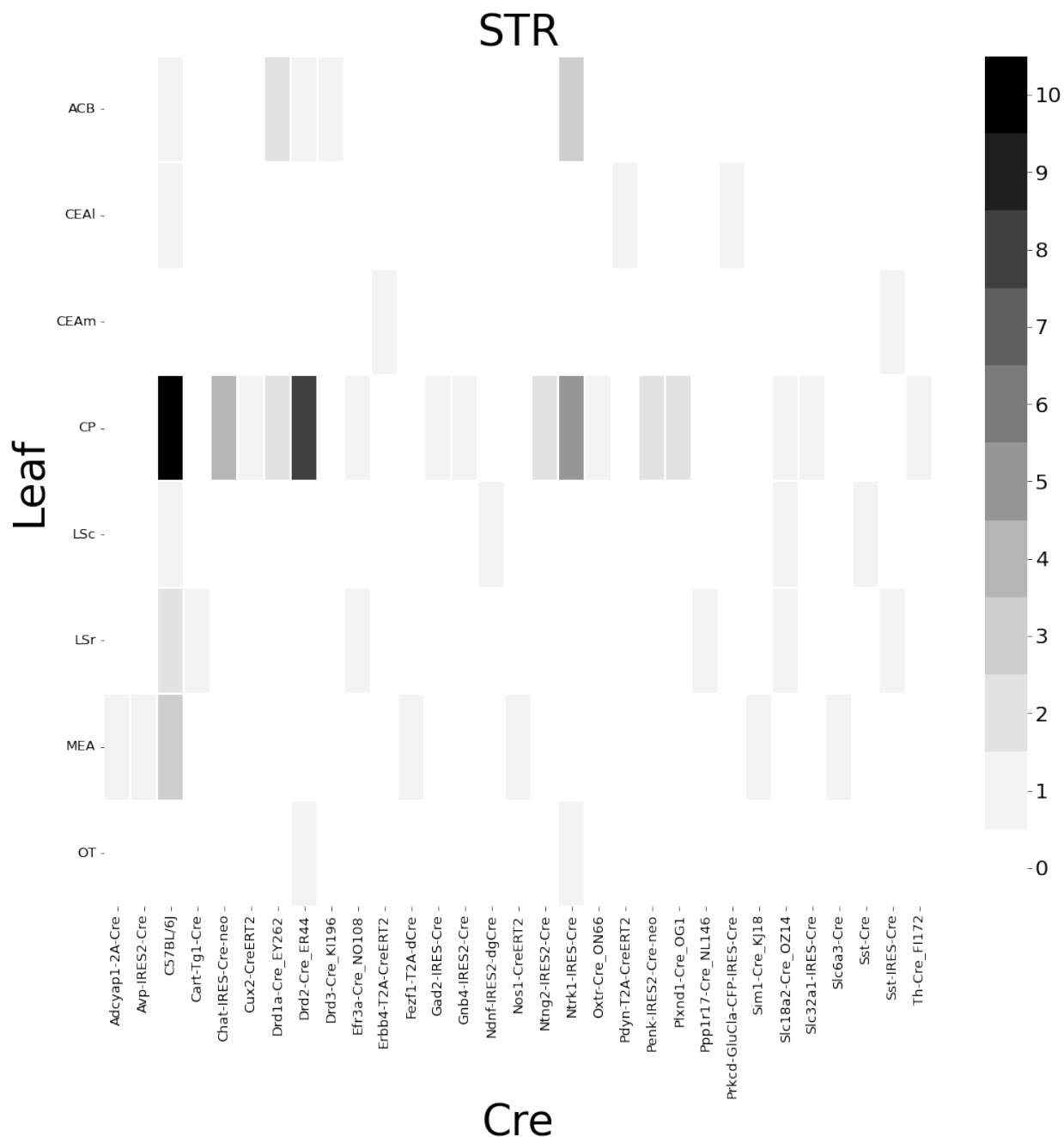


Figure 15: Abundances of Cre-line and leaf-centroid combinations.

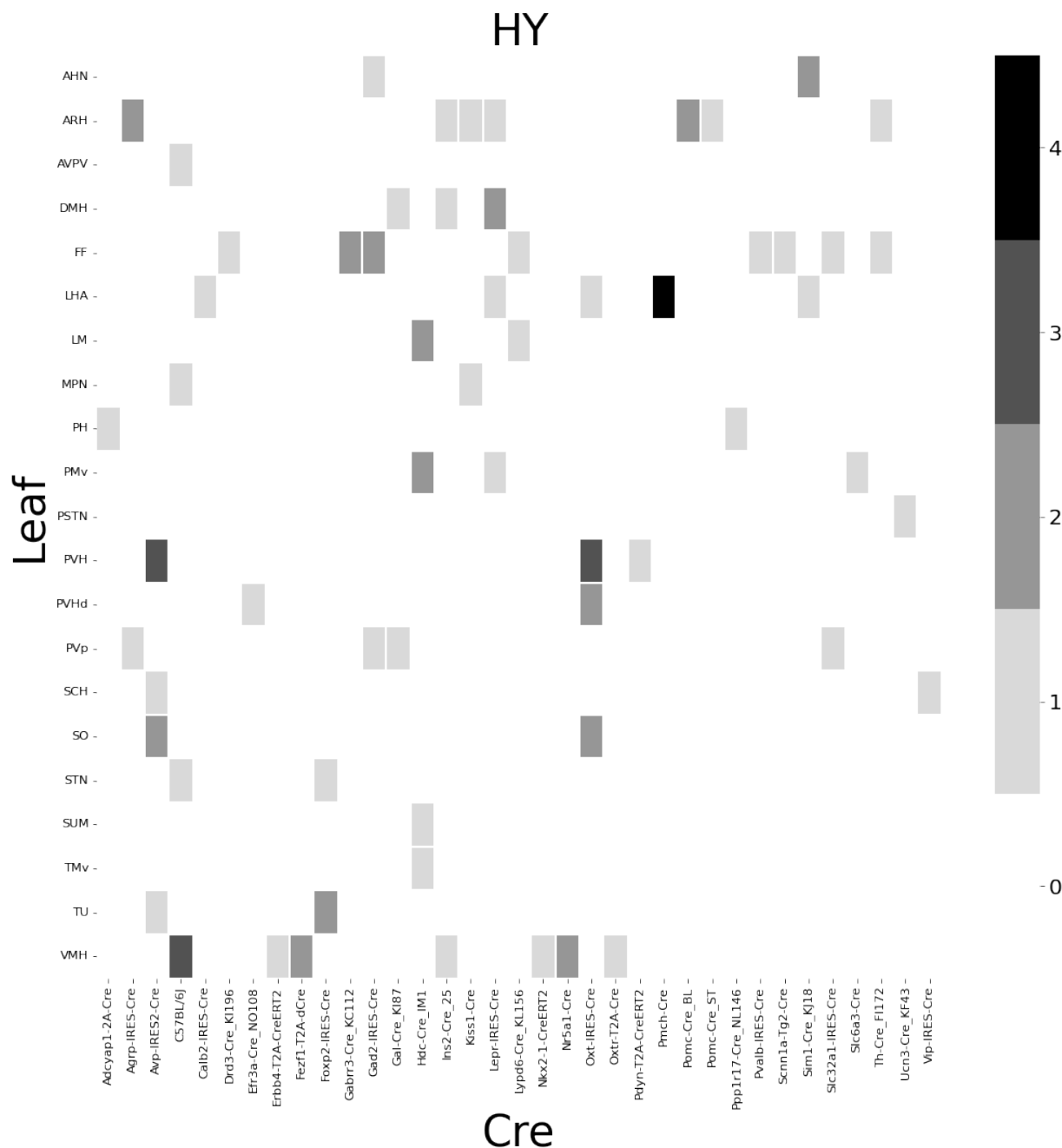


Figure 16: Abundances of Cre-line and leaf-centroid combinations.

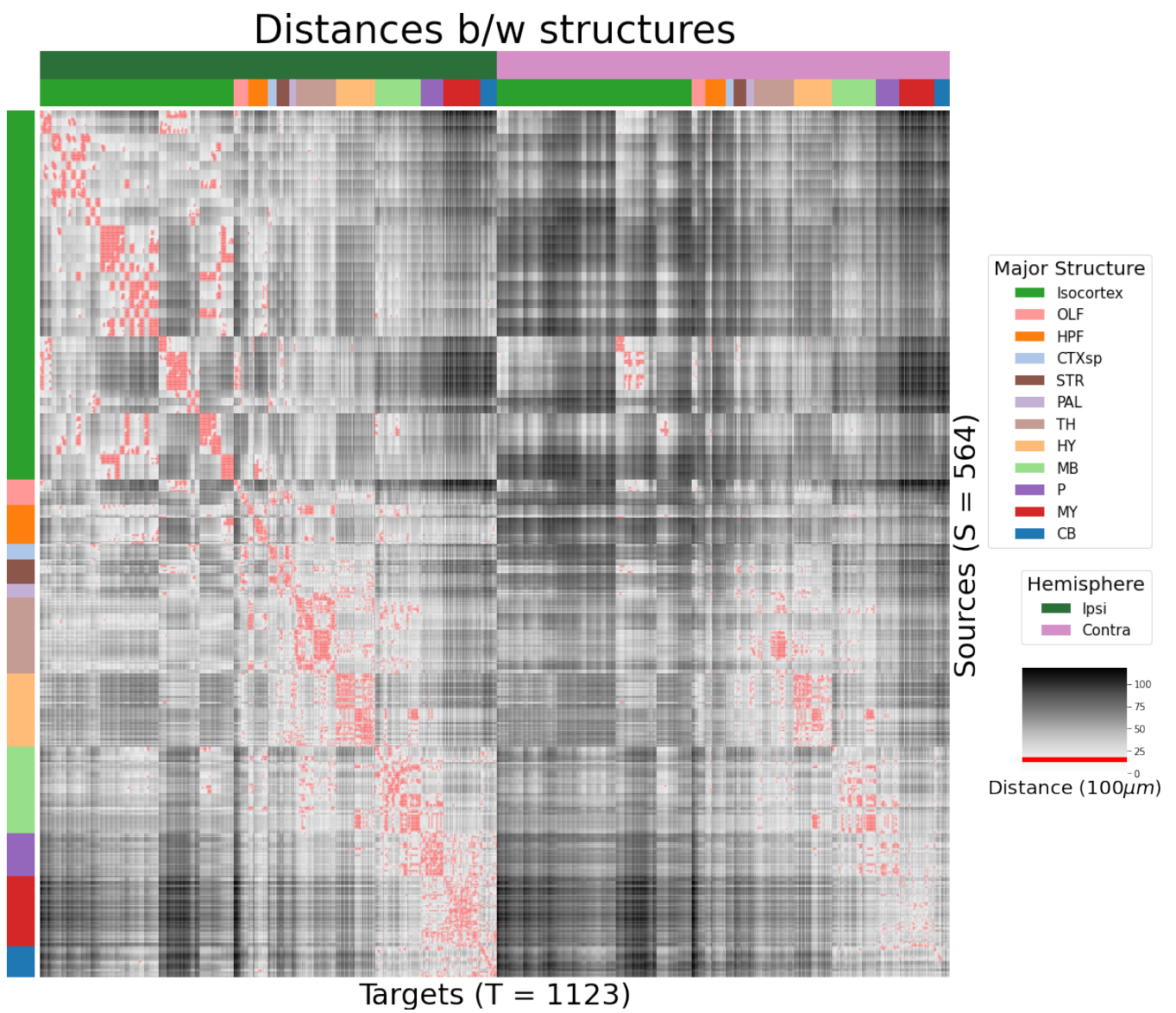
397 ***Distances between structures***

Figure 17: Distance between structures. Short-range connections are masked in red

**398 Model evaluation**

399 We give information on the quality of our models. This includes the sizes of our evaluation sets in  
 400 leave-one-out cross-validation and additional losses in the injection-normalized case.

401 NUMBER OF EXPERIMENTS IN EVALUATION SETS In order to compare between methods, we therefore  
 402 restrict to the smallest set of evaluation indices, which is to say, virus-leaf combinations that are  
 403 present at least twice. This means that our evaluation set is smaller in size than our overall list of  
 404 experiments.

	Total	Cre-Leaf	Cre-leaf over threshold
Isocortex	36	4	4
OLF	7	2	2
HPF	122	62	59
CTXsp	85	41	38
STR	1128	732	7
PAL	68	18	17
TH	46	7	7
HY	35	17	17
MB	33	8	8
P	30	11	11
MY	78	45	44
CB	83	29	29

Table 3: Number of experiments available to evaluate models in leave-one-out cross validation. Models that rely on a finer granularity of modeling have less data available to validate with.

405 INJECTION-NORMALIZED LOSSES To compare with the injection-normalization procedure from ?, we  
 406 also remove experiments with small injection, and here give results for this slightly reduced set using  
 407 injection-normalization. That is, instead of dividing the projection signal of each experiment by its  $l_1$   
 408 norm, we divide by the  $l_1$  norm of the corresponding injection signal. We find that setting a summed  
 409 injection-signal of threshold of 1 is sufficient for evading pathological edge cases in this  
 410 normalization, while still retaining a large evaluation set.

$\hat{f}$	Mean	NW					EL
$\mathcal{D}$	$I_c \cap I_L$	$I_c \cap I_M$	$I_c \cap I_L$	$I_L$	$I_{wt} \cap I_M$	$I_M$	$I_L$
Isocortex	0.413	0.453	0.408	0.538	0.528	0.528	<b>0.396</b>
OLF	0.499	0.504	0.494	0.441	0.543	0.543	<b>0.437</b>
HPF	0.336	0.483	0.332	0.444	0.501	0.501	<b>0.321</b>
CTXsp	0.497	0.497	0.497	0.497	0.497	0.497	0.497
STR	0.359	0.386	0.359	0.364	0.433	0.433	<b>0.322</b>
PAL	0.519	0.497	0.519	0.436	0.459	0.459	<b>0.434</b>
TH	0.769	0.767	0.769	<b>0.514</b>	0.539	0.539	0.556
HY	0.414	0.439	0.414	0.441	0.452	0.452	<b>0.399</b>
MB	0.459	0.396	0.397	0.358	<b>0.324</b>	<b>0.324</b>	0.403
P	<b>0.562</b>	<b>0.562</b>	<b>0.562</b>	0.758	0.764	0.764	<b>0.562</b>
MY	0.699	0.552	0.621	<b>0.439</b>	0.578	0.578	<b>0.439</b>
CB	0.849	0.689	0.849	0.500	0.615	0.615	<b>0.495</b>

Table 4: Losses from leave-one-out cross-validation of candidate for injection-normalized regionalized connectivity on injection-thresholded evaluation set. **Bold** numbers are best for their major structure.

<sup>411</sup> PROJECTION-NORMALIZED LOSSES ON THRESHOLDED SET We also give results for the  
<sup>412</sup> projection-normalization procedure from the main text on this reduced subset.

$\hat{f}$	Mean	NW	EL				
$\mathcal{D}$	$I_c \cap I_L$	$I_c \cap I_M$	$I_c \cap I_L$	$I_L$	$I_{wt} \cap I_M$	$I_M$	$I_L$
Isocortex	0.229	0.248	0.224	0.274	0.269	0.269	<b>0.217</b>
OLF	0.193	0.233	0.191	<b>0.135</b>	0.179	0.179	0.138
HPF	0.178	0.342	<b>0.172</b>	0.212	0.235	0.235	<b>0.172</b>
CTXsp	<b>0.621</b>	<b>0.621</b>	<b>0.621</b>	<b>0.621</b>	<b>0.621</b>	<b>0.621</b>	<b>0.621</b>
STR	0.128	<b>0.117</b>	0.124	0.171	0.234	0.234	0.125
PAL	0.203	0.205	0.203	0.295	0.291	0.291	<b>0.188</b>
TH	0.673	0.664	0.673	<b>0.358</b>	0.379	0.379	0.417
HY	0.358	0.378	0.351	0.331	0.312	<b>0.312</b>	0.314
MB	0.168	0.191	<b>0.160</b>	0.199	0.202	0.202	<b>0.160</b>
P	0.292	0.292	0.292	0.299	0.299	0.299	<b>0.287</b>
MY	0.268	0.347	0.268	<b>0.167</b>	0.189	0.189	0.196
CB	0.062	0.062	0.062	0.068	0.108	0.108	<b>0.061</b>

Table 5: Losses from leave-one-out cross-validation of candidate for normalized regionalized connectivity on injection-thresholded evaluation set. **Bold** numbers are best for their major structure.

## 6 SUPPLEMENTAL METHODS

<sup>413</sup> This section consists of additional information on preprocessing of the neural connectivity data,  
<sup>414</sup> estimation of connectivity, and matrix factorization.

<sup>415</sup> ***Data preprocessing***

<sup>416</sup> Several data preprocessing steps take place prior to evaluations of the connectivity matrices. These  
<sup>417</sup> steps are described in Algorithm PREPROCESS. The arguments of this normalization process - injection  
<sup>418</sup> signals  $x(i)$ , projection signals  $y(i)$ , injection fraction  $F(i)$ , and data quality mask  $q(i)$  - were  
<sup>419</sup> downloaded using the Allen SDK. The injections and projection signals  $\mathcal{B} \rightarrow [0, 1]$  were segmented  
<sup>420</sup> manually in histological analysis. The projection signal gives the proportion of pixels within the voxel  
<sup>421</sup> displaying fluorescence, and the injection signal gives the proportion of pixels within the  
<sup>422</sup> histologically-selected injection subset displaying fluorescence. The injection fraction  $\mathcal{B} \rightarrow [0, 1]$  gives  
<sup>423</sup> the proportion of pixels within each voxel in the injection subset. Finally, the data quality mask  
<sup>424</sup>  $\mathcal{B} \rightarrow \{0, 1\}$  gives the voxels that have valid data.

<sup>425</sup> Our preprocessing makes use of the above ingredients, as well as several other essential steps. First,  
<sup>426</sup> we compute the weighted injection centroid

$$c(i) = \sum_{l \in \mathcal{B}} x(l) l$$

<sup>427</sup> where  $x(i)(l)$  is the injection density at location  $l \in \mathbb{R}^3$ . Given a regionalization  $\mathcal{R}$  from the Allen SDK,  
<sup>428</sup> we can also access regionalization map  $R: \mathcal{B} \rightarrow \mathcal{R}$ . This induces a functional of connectivities from  
<sup>429</sup> the space of maps  $\{\mathcal{X} = x: \mathcal{B} \rightarrow [0, 1]$

$$\begin{aligned} 1_{\mathcal{R}}: \mathcal{X} &\rightarrow \mathcal{R} \times \mathbb{R}_{\geq 0} \\ x &\mapsto \sum_{l \in r} x(l) \text{ for } r \in \mathcal{R}. \end{aligned}$$

<sup>430</sup> We also can restrict a signal to a individual structure as

$$\begin{aligned} 1|_s: \mathcal{X} &\rightarrow \mathcal{X} \\ x(l) &= \begin{cases} x(l) & \text{if } l \in S \\ 0 & \text{otherwise.} \end{cases} \end{aligned}$$

<sup>431</sup> Finally, given a vector or array  $a \in \mathbb{R}^T$ , we have the  $l1$  normalization map

$$n: a \mapsto \frac{a}{\sum_{j=1}^T a_j}.$$

<sup>432</sup> We define these objects as functions and functionals, but this is for notational convenience and

<sup>433</sup> non-essential. A function  $x(i) : \mathcal{B} \rightarrow [0, 1]$  is mathematically equivalent to the graph

<sup>434</sup>  $\mathcal{G}(x(i)) \in \mathcal{B} \times [0, 1]$ . As an abuse of notation, we define  $x \odot x' := z$  such that  $z(l) = x(l)x'(l)$  for all  $l \in \mathcal{B}$ .

<sup>435</sup> Also, denote  $m(i)$  as the major structure containing experiment  $i$ . We then can write the

<sup>436</sup> preprocessing algorithm.

---

**PREPROCESS 1 Input** Injection  $x$ , Projection  $y$ , Injection centroid  $c \in \mathbb{R}^3$ , Injection fraction  $F$ , data quality mask  $q$

---

Injection fraction  $x_F \leftarrow x \odot F$

Data-quality censor  $y_q \leftarrow y \odot q$ ,  $x_q \leftarrow x_F \odot q$

Restrict injection  $x_m = 1|_m x_q$ .

Compute centroid  $c$  from  $x_m$

Regionalize  $\tilde{y}_{\mathcal{T}} \leftarrow 1_{\mathcal{T}}(y_q)$

Normalize  $y_{\mathcal{T}} \leftarrow n(\tilde{y}_{\mathcal{T}})$

---

**Output**  $\tilde{y}_{\mathcal{T}}, c$

---

437 **Estimators**

438 As mentioned previously, we can consider our estimators as modeling a connectivity vector  
 439  $f_{\mathcal{T}}(v, s) \in \mathbb{R}_{\geq 0}^T$ . Thus, for the remainder of this section, we will discuss only  $f(v, s)$ . We review the  
 440 Nadaraya-Watson estimator from ?, and describe its conversion into our cell-class specific Expected  
 441 Loss estimator.

442 *Centroid-based Nadaraya-Watson* In the Nadaraya-Watson approach of ?, the injection is considered  
 443 only through its centroid  $c(i)$ , and the projection is considered regionalized. That is,

$$f_*(i) = \{c(i), y_{\mathcal{T}}(i)\}.$$

444 Since the injection is considered only by its centroid, this model only generates predictions for  
 445 particular locations  $l$ , and the prediction for a structure  $s$  is given by integrating over locations within  
 446 the structure

$$f^*(\hat{f}(f_*(\mathcal{D})))(\nu, s) = \sum_{l \in s} \hat{f}(f_*(\mathcal{D}(I)))(\nu, l).$$

447 Here,  $I$  is the training data, and  $\hat{f}$  is the Nadaraya-Watson estimator

$$\hat{f}_{NW}(c(I), y_{\mathcal{T}}(I))(l) := \sum_{i \in I} \frac{\omega_{il}}{\sum_{i \in I} \omega_{il}} y_{\mathcal{T}}(i)$$

448 where  $\omega_{il} := \exp(-\gamma d(l, c(i))^2)$  and  $d$  is the Euclidean distance between centroid  $c(i)$  and voxel with  
 449 position  $l$ .

450 Several facets of the estimator are visible here. A smaller  $\gamma$  corresponds to a greater amount of  
 451 smoothing, and the index set  $I \subseteq \{1 : n\}$  generally depends on  $s$  and  $\nu$ . Varying  $\gamma$  bridges between  
 452 1-nearest neighbor prediction and averaging of all experiments in  $I$ . In ?,  $I$  consisted of experiments  
 453 sharing the same brain division, i.e.  $I = I_m$ , while restricting of index set to only include experiments  
 454 with the same cell class gives the class-specific Cre-NW model. Despite this restriction, we fit  $\gamma$  by  
 455 leave-one-out cross-validation for each  $m$  rather than a smaller subset like  $s$  or  $\nu$ . That is,

$$\hat{\gamma}_m = \arg \min_{\gamma \in \mathbb{R}_{\geq 0}} \frac{1}{|\{s, \nu\}|} \sum_{s, \nu \in \{m, \mathcal{V}\}} \frac{1}{|I_s \cap I_\nu|} \sum_{i \in (I_s \cap I_\nu)} \ell(y_{\mathcal{T}}(i)), \hat{f}_{\mathcal{T}}(f_*(\mathcal{D}(\nu, s) \setminus i)). \quad (2)$$

<sup>456</sup> *The Expected-Loss estimator* Besides location of the injection centroid, cell class also influences  
<sup>457</sup> projection. Thus, we introduce method for estimating the effect of Cre-distance, which we define as  
<sup>458</sup> the distance between the projections of the mean experiment of one (Cre,leaf) pair with another. This  
<sup>459</sup> method assigns a predictive weight to each pair of training points that depends both on their  
<sup>460</sup> centroid-distance and Cre-distance. This weight is determined by the expected prediction error of  
<sup>461</sup> each of the two feature types

<sup>462</sup> We define Cre-line behavior as the average regionalized projection of a Cre-line in a given structure  
<sup>463</sup> (i.e. leaf). The vectorization of categorical information is known as **target encoding**

$$\bar{y}_{\mathcal{T},s,v} := \frac{1}{|I_s \cap I_v|} \sum_{i \in (I_s \cap I_v)} y_{\mathcal{T}}(i)$$

<sup>464</sup> The Cre-distance is then defined a **Cre-distance** in a leaf to be the distance between the target-encoded  
<sup>465</sup> projections of two Cre-lines. The relative predictive accuracy of Cre-distance and centroid distance is  
<sup>466</sup> determined by fitting a surface of projection distance as a function of Cre-distance and centroid  
<sup>467</sup> distance.

<sup>468</sup> as determined by cross-validation. When we use shape-constrained B-splines to estimate this  
<sup>469</sup> weight, the weights then may be said to be used in a Nadaraya-Watson estimator.

<sup>470</sup> For this reason, we call this the Expected Loss Estimator. The resulting weights are then utilized in a  
<sup>471</sup> Nadaraya-Watson estimator in a final prediction step. increase the effective sample size of our  
<sup>472</sup> Nadaraya-Watson estimator,

<sup>473</sup> In mathematical terms, our full feature set consists of the centroid coordinates and the  
<sup>474</sup> target-encoded means of the combinations of virus type and injection-centroid structure. That is,

$$f_*(\mathcal{D}_i) = \{c(i), \{\bar{y}_{\mathcal{T},s,v} \forall v\}, y_{\mathcal{T}}(i)\}.$$

<sup>475</sup>  $f^*$  is defined as in (??). The expected loss estimator is then

$$\hat{f}_{EL}(c(I), y_{\mathcal{T}}(I))(l, v) := \sum_{i \in I} \frac{v_{ilv}}{\sum_{i \in I} v_{ilv}} y_{\mathcal{T}}(i)$$

<sup>476</sup> where

$$v_{ilv} := \exp(-\gamma g(d(l, c(i))^2, d(\bar{y}_{\mathcal{T},s,v}, \bar{y}_{\mathcal{T},s,v(i)})^2))$$

<sup>477</sup> and  $s$  is the structure containing  $l$ .

<sup>478</sup> The key step therefore is finding a suitable function  $g$  with which to weight the positional and Cre  
<sup>479</sup> information. Note that  $g$  must be a concave, non-decreasing function of its arguments with with  
<sup>480</sup>  $g(0, 0) = 0$ . Then,  $g$  defines a metric on the product of the metric spaces defined by experiment  
<sup>481</sup> centroid and target-encoded cre-line, and  $\hat{f}_{EL}$  is a Nadaraya-Watson estimator. A derivation of this  
<sup>482</sup> fact is given later in this section.

<sup>483</sup> We therefore use a linear generalized additive model of shape-constrained B-splines to estimate  $g$   
<sup>484</sup> (?). This is a method for generating a predictive model  $g$  that minimizes the loss of

$$\sum_{i, i' \in S} \| \|y_{\mathcal{T}}(i) - y_{\mathcal{T}}(i')\|_2 - \sum_{q=1}^Q \rho_q B_q(\|c(i') - c(i)\|_2, \|\bar{y}_{\mathcal{T}, s, v} - \bar{y}_{\mathcal{T}, s, v}(i)\|) \|_2$$

<sup>485</sup> given the constraints on  $g$ . That is, given all pairs of experiments with injection centroid in the same  
<sup>486</sup> structure,  $g$  gives a prediction of the distance between their projections made using the distance  
<sup>487</sup> between the average behavior of their Cre-lines given their injection centroid, and the distance  
<sup>488</sup> between their injection centroids. In particular,  $g$  is the empirically best such function within the  
<sup>489</sup> class of  $B$ -splines, which Similarly to the Nadaraya-Watson model, we make the decision to fit a  $g$   
<sup>490</sup> separately for each major brain division, and select  $\hat{\gamma}$  as in ???. We set  $Q = 10$  and leave validation of  
<sup>491</sup> this parameter, as well as the precise nature of the polynomial  $B$ -spline terms  $B_q$  out of the scope of  
<sup>492</sup> this paper. Empirically this leads to a smooth surface using the pyGAM Python package (?).

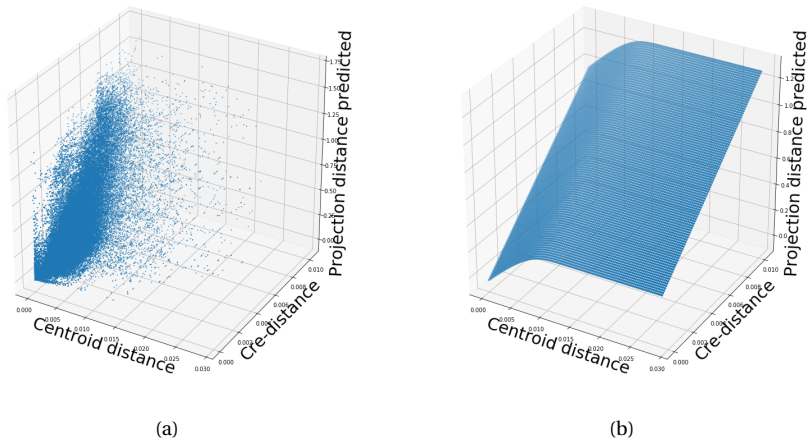


Figure 18: Fitting  $g$ . ?? Distribution of projection errors against centroid distance and cre-distance in Isocortex. ?? estimated  $\hat{g}$  using B-splines.

493 JUSTIFICATION OF SHAPE CONSTRAINT    The shape-constrained expected-loss estimator introduced  
 494 in this paper is, to our knowledge, novel. It should be considered an alternative method to the classic  
 495 weighted kernel method. While we do not attempt a detailed theoretical study of this estimator, we do  
 496 establish the need for the shape constraint in our spline estimator. Though this fact is probably well  
 497 known, we prove a (slightly stronger) version here for completeness.

498 **Proposition 1.** *Given a collection of metric spaces  $X_1, \dots, X_n$  with metrics  $d_1, \dots, d_n$  (e.g.  $d_{centroid}, d_{cre}$ ),  
 499 and a function  $f : (X_1 \times X_1) \dots \times (X_n \times X_n) = g(d_1(X_1 \times X_1), \dots, d_n(X_n \times X_n))$ , then  $f$  is a metric if  $g$  is  
 500 concave, non-decreasing and  $g(d) = 0 \iff d = 0$ .*

501 *Proof.* We show  $g$  satisfying the above properties implies that  $f$  is a metric.

- 502    ▪ The first property of a metric is that  $f(x, x') = 0 \iff x = x'$ . The left implication:  
 503        $x = x' \implies f(x_1, x'_1, \dots, x_n, x'_n) = g(0, \dots, 0)$ , since  $d$  are metrics. Then, since  $g(0) = 0$ , we have that  
 504        $f(x, x') = 0$ . The right implication:  $f(x, x') = 0 \implies d = 0 \implies x = x'$  since  $d$  are metrics.
- 505    ▪ The second property of a metric is that  $f(x, x') = f(x', x)$ . This follows immediately from the  
 506       symmetry of the  $d_i$ , i.e.  $f(x, x') = f(x_1, x'_1, \dots, x_n, x'_n) = g(d_1(x_1, x'_1), \dots, d_n(x_n, x'_n)) =$   
 507        $g(d_1(x'_1, x_1), \dots, d_n(x'_n, x_n)) = f(x'_1, x_1, \dots, x'_n, x_n) = f(x', x)$ .
- 508    ▪ The third property of a metric is the triangle inequality:  $f(x, x') \leq f(x, x^*) + f(x^*, x')$ . To show this  
 509       is satisfied for such a  $g$ , we first note that  $f(x, x') = g(d(x, x')) \leq g(d(x, x^*) + d(x^*, x'))$  since  $g$  is  
 510       non-decreasing and by the triangle inequality of  $d$ . Then, since  $g$  is concave,  
 511        $g(d(x, x^*) + d(x^*, x')) \leq g(d(x, x^*)) + g(d(x^*, x')) = f(x, x^*) + f(x^*, x')$ .

513 ***Setting a lower detection threshold***

514 The lower detection threshold of our approach is a complicated consequence of our experimental and  
 515 analytical protocols. For example, the Nadaraya-Watson estimator is likely to generate many small  
 516 false positive connections, since the projection of even a single experiment within the source region  
 517 to a target will cause a non-zero connectivity in the Nadaraya-Watson weighted average. On the other  
 518 hand, the complexities of the experimental protocol itself and the image analysis and alignment can  
 519 also cause spurious signals. Therefore, it is of interest to establish a lower-detection threshold below  
 520 which we have very little power-to-predict, and set estimated connectivities below this threshold to  
 521 zero.

522 We set this threshold with respect to the sum of Type 1 and Type 2 errors

$$\iota = \sum_{i \in \mathcal{E}} 1_{y_{\mathcal{T}}^T(i)=0}^T 1_{\hat{f}_{\mathcal{T}}(\nu(i), c(i)) > \tau} + 1_{y_{\mathcal{T}}^T(i) > 0}^T 1_{\hat{f}_{\mathcal{T}}(\nu(i), c(i)) < \tau}.$$

523 We then select the  $\tau$  that minimizes  $\iota$ . Results for this approach are given in Supplemental Section

524 ??.

525 ***Decomposing the connectivity matrix***

526 We utilize non-negative matrix factorization (NMF) to analyze the principal signals in our  
 527 connectivity matrix. Here, we review this approach as applied to decomposition of the distal elements  
 528 of the estimated connectivity matrix  $\hat{\mathcal{C}}$  to identify  $q$  connectivity archetypes. Aside from the NMF  
 529 program itself, the key elements are selection of the number of archetypes  $q$  and stabilization of the  
 530 tendency of NMF to give random results over different initializations.

531 *Non-negative matrix factorization* As discussed in ?, one of the most basic processes underlying the  
 532 observed connectivity is the tendency of each source region to predominantly project to proximal  
 533 regions. For example, the heatmap in Supplemental Figure 17 shows that the pattern of intrastructure  
 534 distances resembles the connectivity matrix in ?. These connections are biologically meaningful, but  
 535 also unsurprising, and their relative strength biases learned latent coordinate representations away  
 536 from long-range structures. For this reason, we establish a  $1500\mu\text{m}$  'distal' threshold within which to  
 537 exclude connections for our analysis.

538 Given a matrix  $X \in \mathbb{R}_{\geq 0}^{a \times b}$  and a desired latent space dimension  $q$ , the non-negative matrix  
 539 factorization is thus

$$\text{NMF}(\mathcal{C}, \lambda, q, \mathbf{1}_M) = \arg \min_{W \in \mathbb{R}_{\geq 0}^{S \times q}, H \in \mathbb{R}_{\geq 0}^{q \times T}} \frac{1}{2} \|\mathbf{1}_M \odot \mathcal{C} - WH\|_2^2 + \lambda(\|H\|_1 + \|W\|_1).$$

540 The mask  $\mathbf{1}_M$  specifies this objective for detecting patterns in long-range connections. We note the  
 541 existence of NMF with alternative norms for certain marginal distributions, but leave utilization of  
 542 this approach for future work (?).

543 The mask  $\mathbf{1}_M \in \{0, 1\}^{S \times T}$  serves two purposes. First, it enables computation of the NMF objective  
 544 while excluding self and nearby connections. These connections are both strong and linearly  
 545 independent, and so would unduly influence the *NMF* reconstruction error over more biologically  
 546 interesting or cell-type dependent long-range connections. Second, it enables cross-validation based  
 547 selection of the number of retained components.

548 *Cross-validating NMF* We review cross-validation for NMF following (?). In summary, a NMF model is  
 549 first fit on a reduced data set, and an evaluation set is held out. After random masking of the  
 550 evaluation set, the loss of the learned model is then evaluated on the basis of successful  
 551 reconstruction of the held-out values. This procedure is performed repeatedly, with replicates of  
 552 random masks at each tested dimensionality  $q$ . This determines the point past which additional  
 553 hidden units provide no additional value for reconstructing the original signal.

554 The differentiating feature of cross-validation for NMF compared with supervised learning is the  
 555 randomness of the masking matrix  $1_M$ . Cross-validation for supervised learning generally leaves out  
 556 entire observations, but this is insufficient for our situation. This is because, given  $W$ , our  $H$  is the  
 557 solution of a regularized non-negative least squares optimization problem

$$H := \hat{e}_W(1_M \odot \mathcal{C}) = \arg \min_{\beta \in \mathbb{R}_{\geq 0}^{q \times T}} \|1_M \odot \mathcal{C} - W\beta\|_2^2 + \|\beta\|_1. \quad (3)$$

558 The negative effects of an overfit model can therefore be optimized away from on the evaluation set.

A standard solution is to generate uniformly random masks  $1_{M(p)} \in \mathbb{R}^{S \times T}$  where

$$1_{M(p)}(s, t) \sim \text{Bernoulli}(p).$$

NMF is then performed using the mask  $1_{M(p)}$  to get  $W$ . The cross-validation error is then

$$\epsilon_q = \frac{1}{R} \sum_{r=1}^R (\|1_{M(p)_r^c} \odot X - W(\hat{e}_W(1_{M(p)_r^c} \odot X))\|_2^2$$

where  $1_{M(p)_r}^c$  is the binary complement of  $1_{M(p)_r}$  and  $R$  is a number of replicates. Theoretically, the optimum number of components is then

$$\hat{q} = \operatorname{arg\,min}_q \epsilon_q.$$

559 *Stabilizing NMF* The NMF program is non-convex, and, empirically, individual replicates will not  
 560 converge to the same optima. One solution therefore is to run multiple replicates of the NMF  
 561 algorithm and cluster the resulting vectors. This approach raises the questions of how many clusters  
 562 to use, and how to deal with stochasticity in the clustering algorithm itself. We address this issue  
 563 through the notion of clustering stability (?).

The clustering stability approach is to generate  $L$  replicas of k-cluster partitions  $\{C_{kl} : l \in 1 \dots L\}$  and then compute the average dissimilarity between clusterings

$$\xi_k = \frac{2}{L(L-1)} \sum_{l=1}^L \sum_{l'=1}^l d(C_{kl}, C_{kl'}).$$

Then, the optimum number of clusters is

$$\hat{k} = \arg \min_k \xi_k.$$

564 A review of this approach is found in ?. Intuitively, archetype vectors that cluster together frequently  
 565 over clustering replicates indicate the presence of a stable clustering. For  $d$ , we utilize the adjusted  
 566 Rand Index - a simple dissimilarity measure between clusterings. Note that we expect to select slightly  
 567 more than the  $q$  components suggested by cross-validation, since archetype vectors which appear in  
 568 one NMF replicate generally should appear in others. We then select the  $q$  clusters with the most  
 569 archetype vectors - the most stable NMF results - and take the median of each cluster to create a  
 570 sparse representative archetype ?.?. We then find the according  $H$  using Program ?.?. Experimental  
 571 results for these cross-validation and stability selection approaches are given in Supplemental Section  
 572 ??.

## 7 SUPPLEMENTAL EXPERIMENTS

### 573 Setting detection threshold $\tau$

574 We give results on the false detection rate at different limits of detection. These conclusively show that  
 575  $10^{-6}$  is the good threshold for our normalized data.

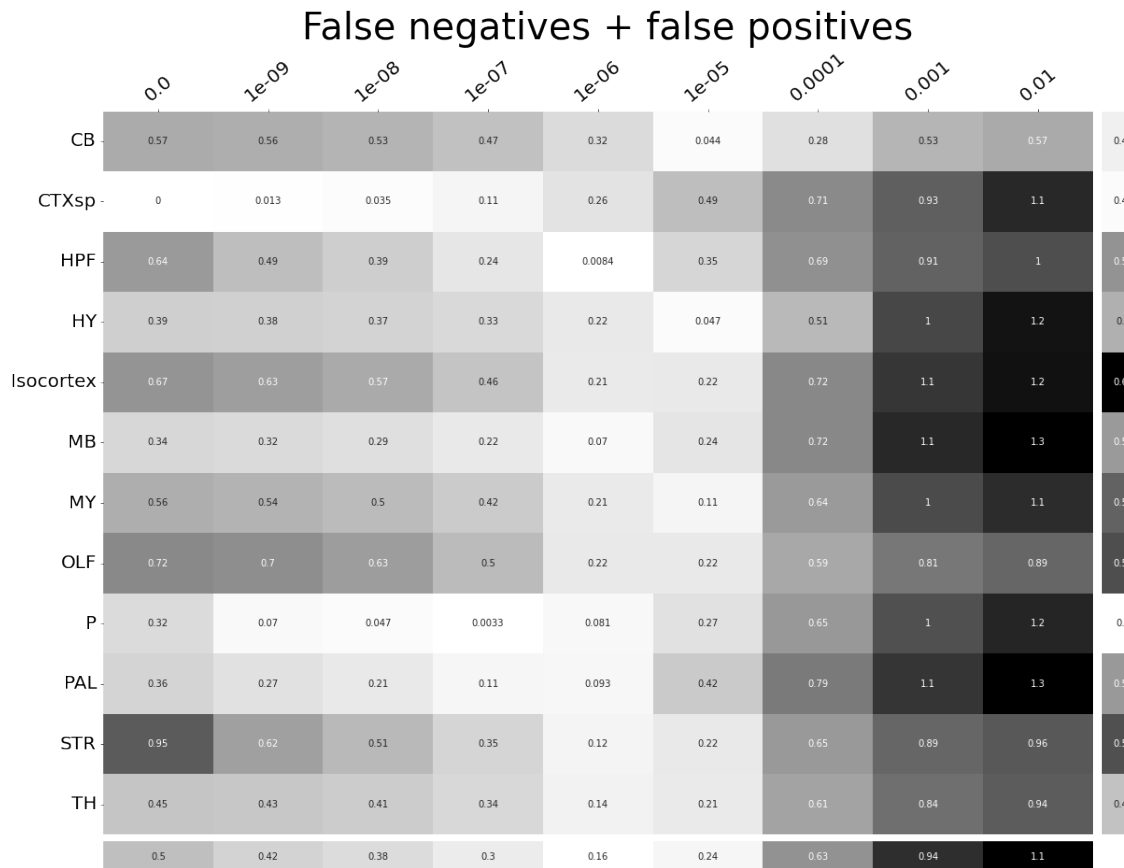


Figure 19:  $\tau$  at different limits of detection in different major structures.  $10^{-6}$  is the optimal detection threshold.

576 ***Loss subsets***

577 We report model accuracies for our *EL* model by neuron class and structure. These expand upon the  
 578 results in Table 2a and give more specific information about the quality of our estimates. CTXsp is  
 579 omitted due to the small nature of the evaluation set.

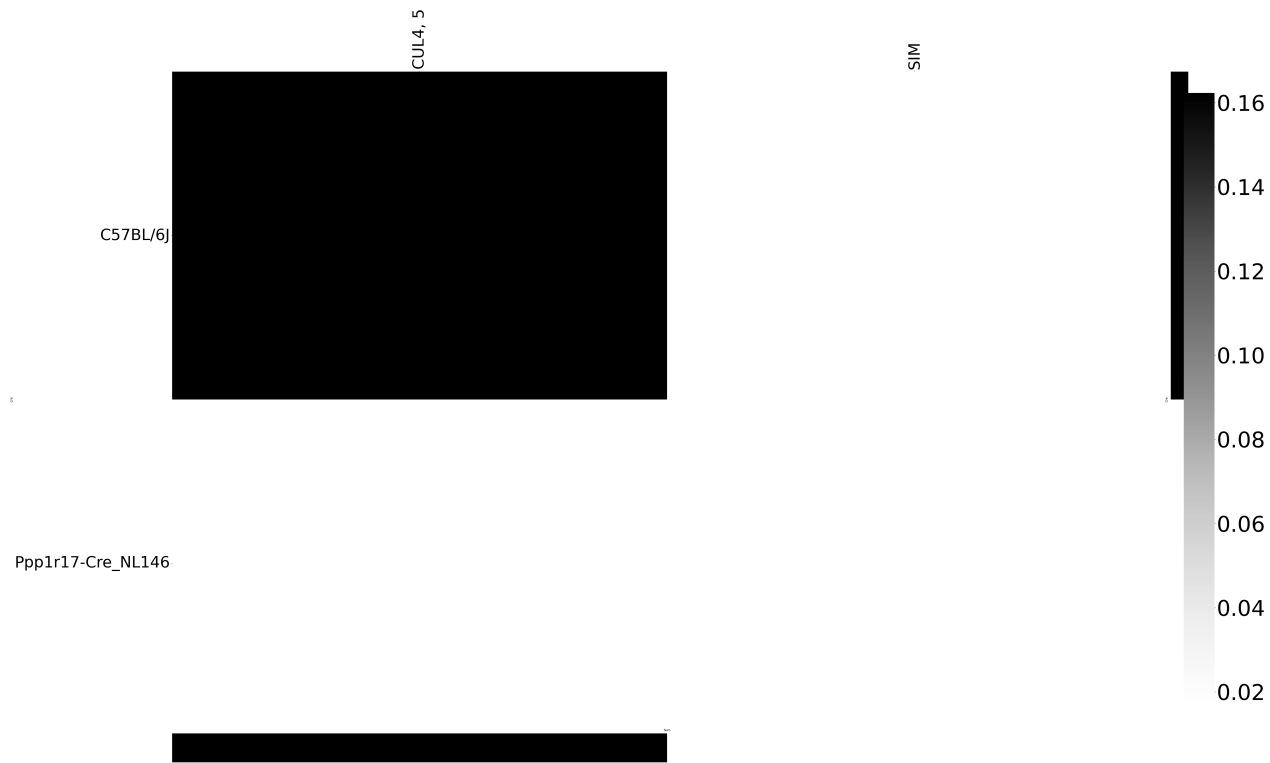


Figure 20: Weighted loss for cre-leaf combinations in CB. Missing values are omitted. Row and column averages are also plotted.

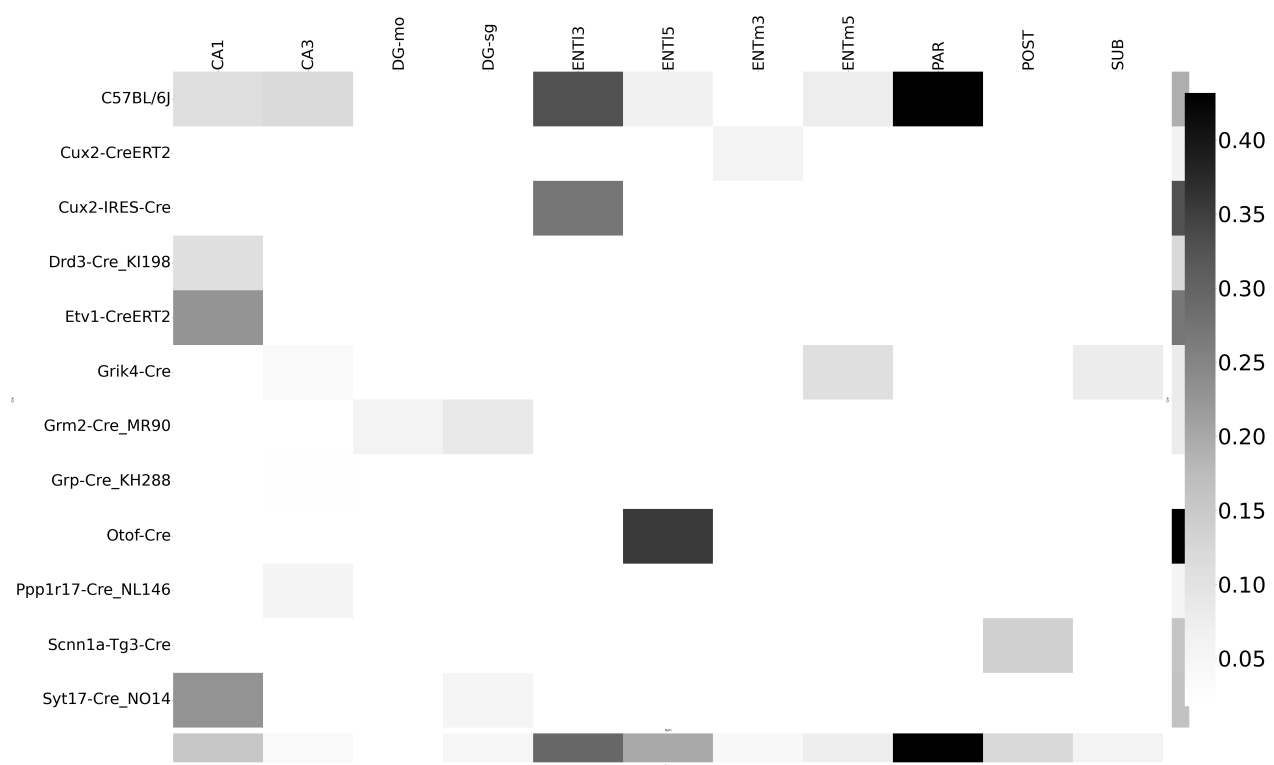


Figure 21: Weighted loss for cre-leaf combinations in HPF. Missing values are omitted. Row and column averages are also plotted.

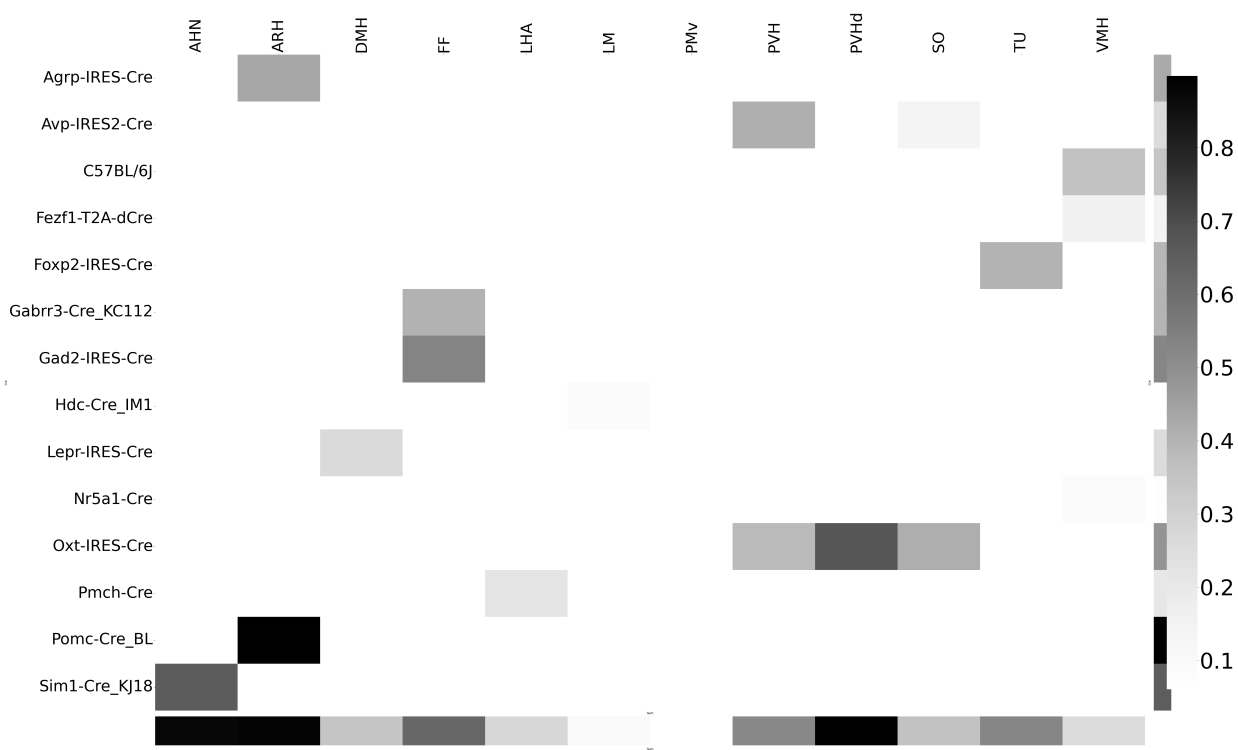


Figure 22: Weighted loss for cre-leaf combinations in HY. Missing values are omitted. Row and column averages are also plotted.

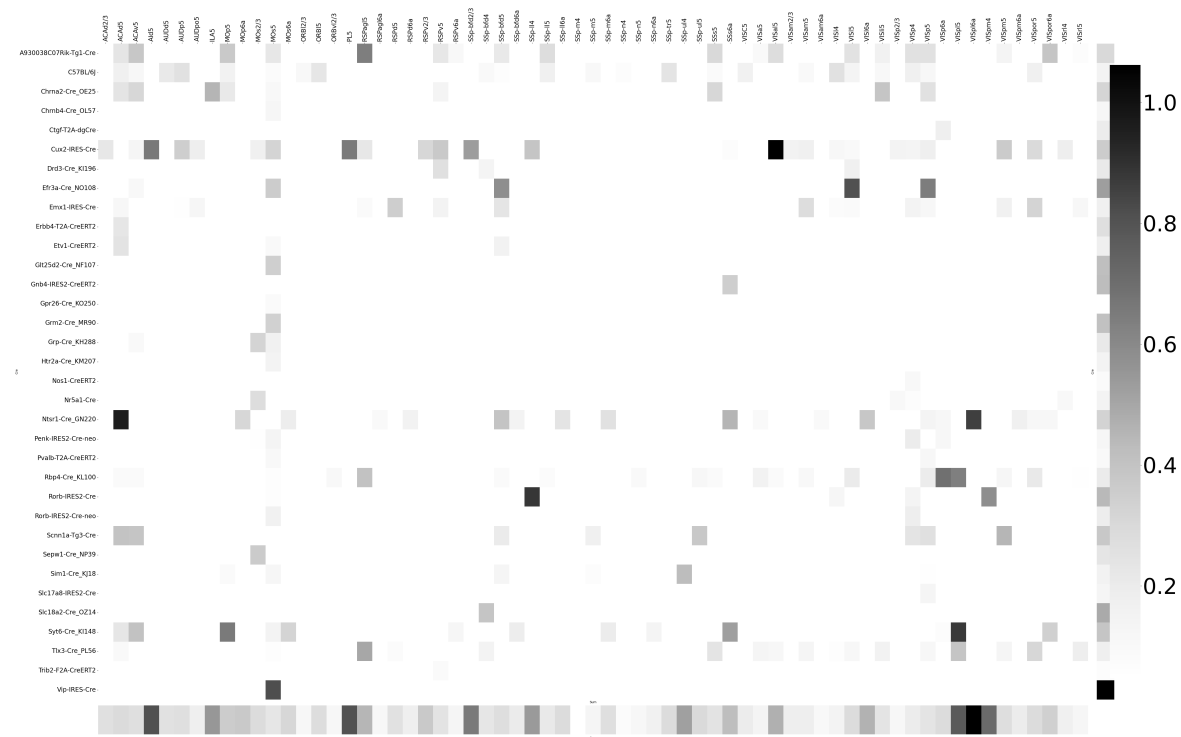


Figure 23: Weighted loss for cre-leaf combinations in Isocortex. Missing values are omitted. Row and column averages are also plotted.

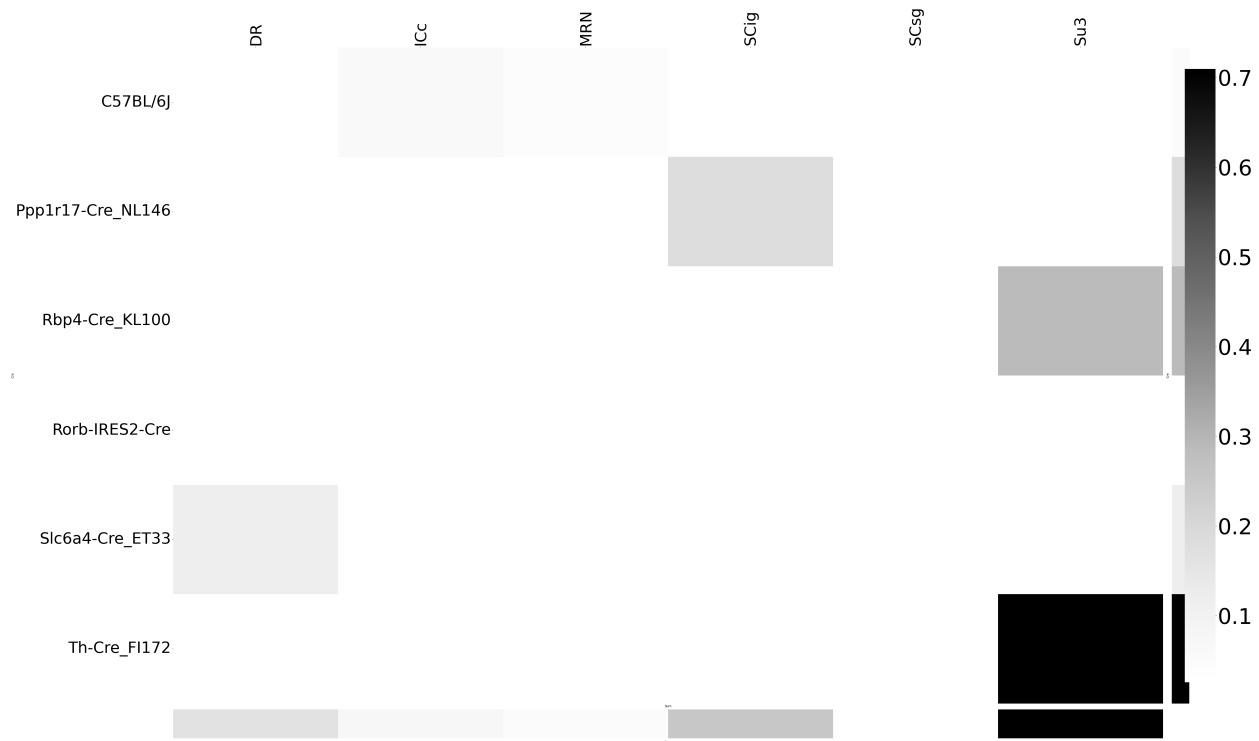


Figure 24: Weighted loss for cre-leaf combinations in MB. Missing values are omitted. Row and column averages are also plotted.

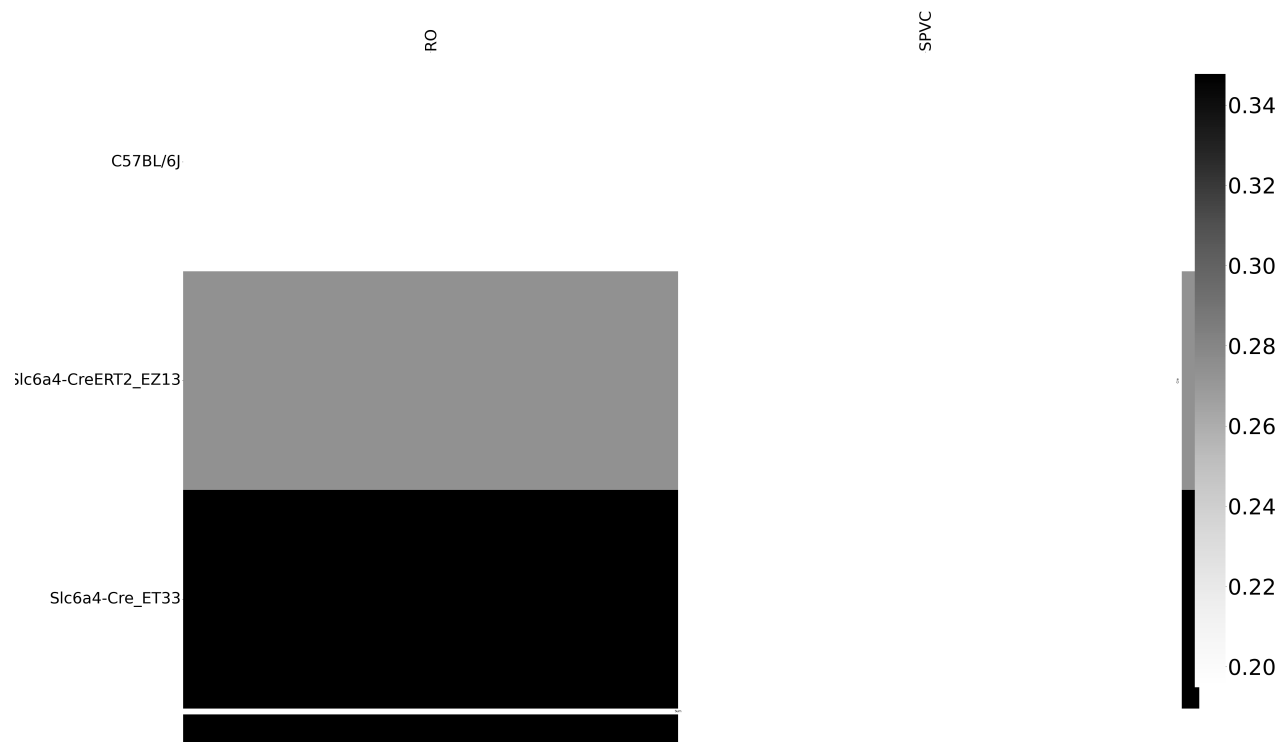


Figure 25: Weighted loss for cre-leaf combinations in MY. Missing values are omitted. Row and column averages are also plotted.

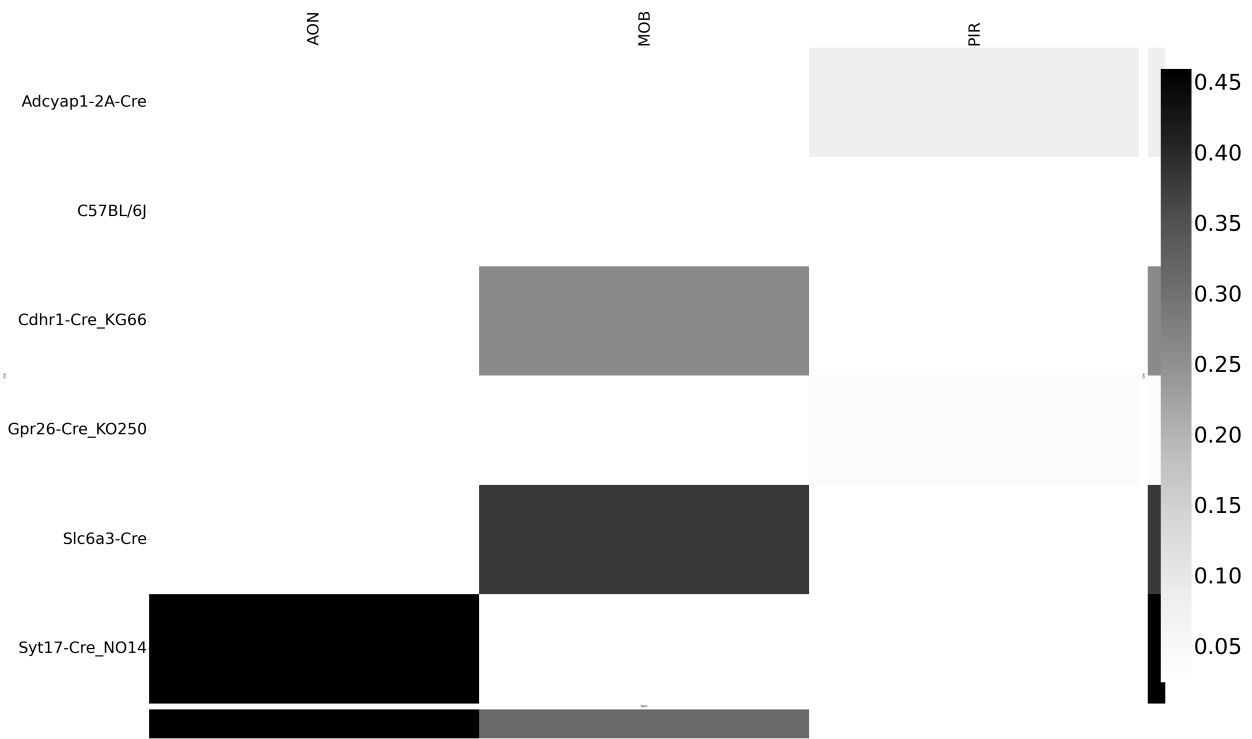


Figure 26: Weighted loss for cre-leaf combinations in OLF. Missing values are omitted. Row and column averages are also plotted.

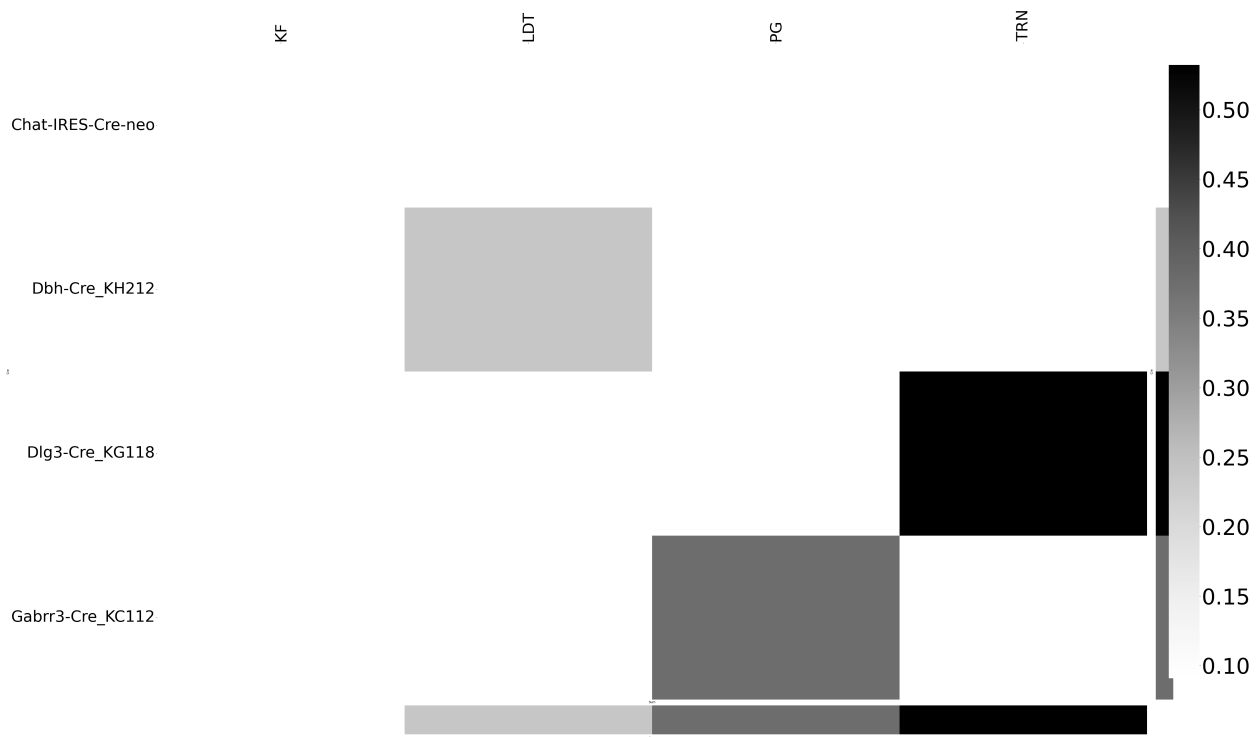


Figure 27: Weighted loss for cre-leaf combinations in P. Missing values are omitted. Row and column averages are also plotted.

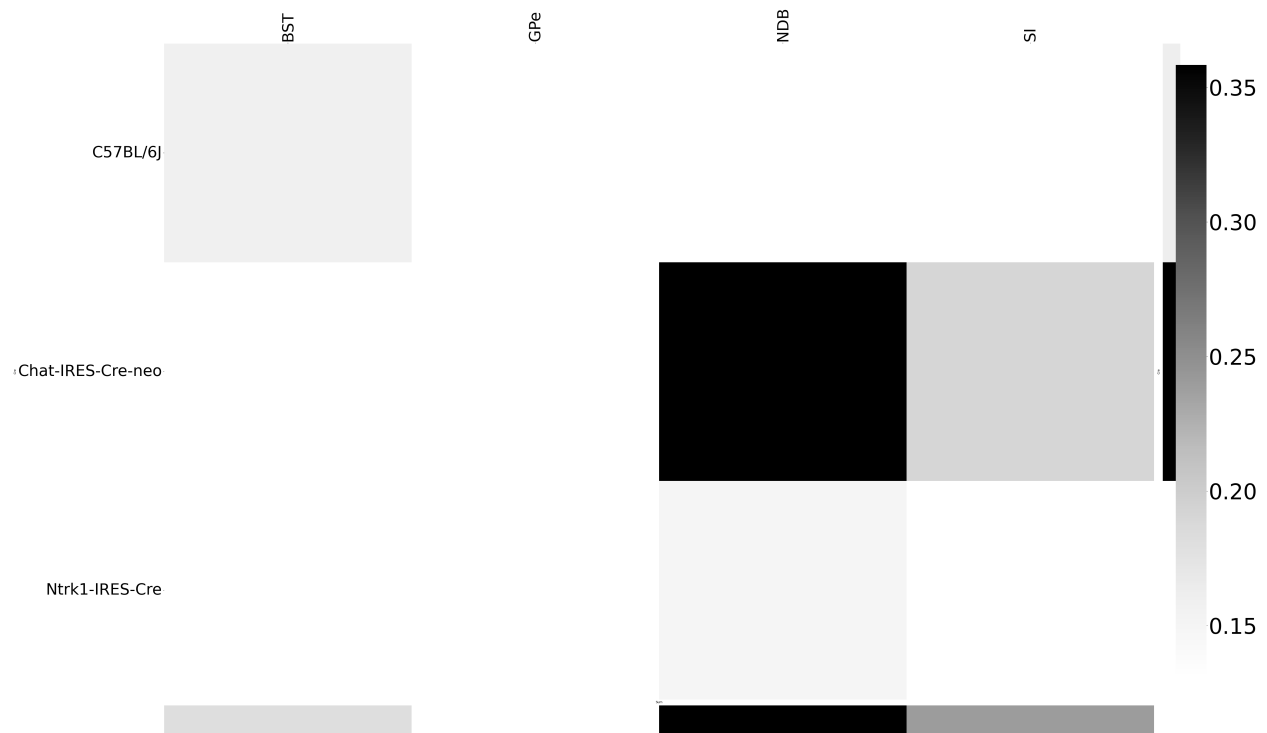


Figure 28: Weighted loss for cre-leaf combinations in PAL. Missing values are omitted. Row and column averages are also plotted.

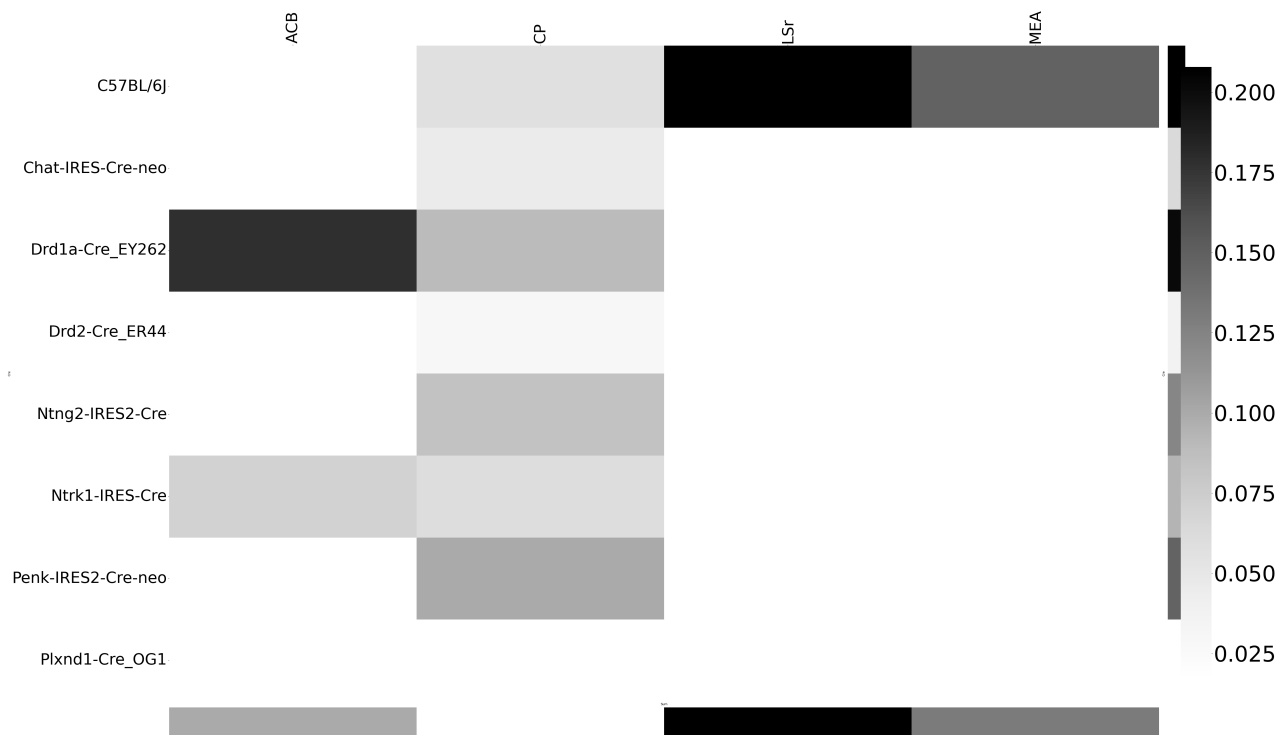


Figure 29: Weighted loss for cre-leaf combinations in STR. Missing values are omitted. Row and column averages are also plotted.

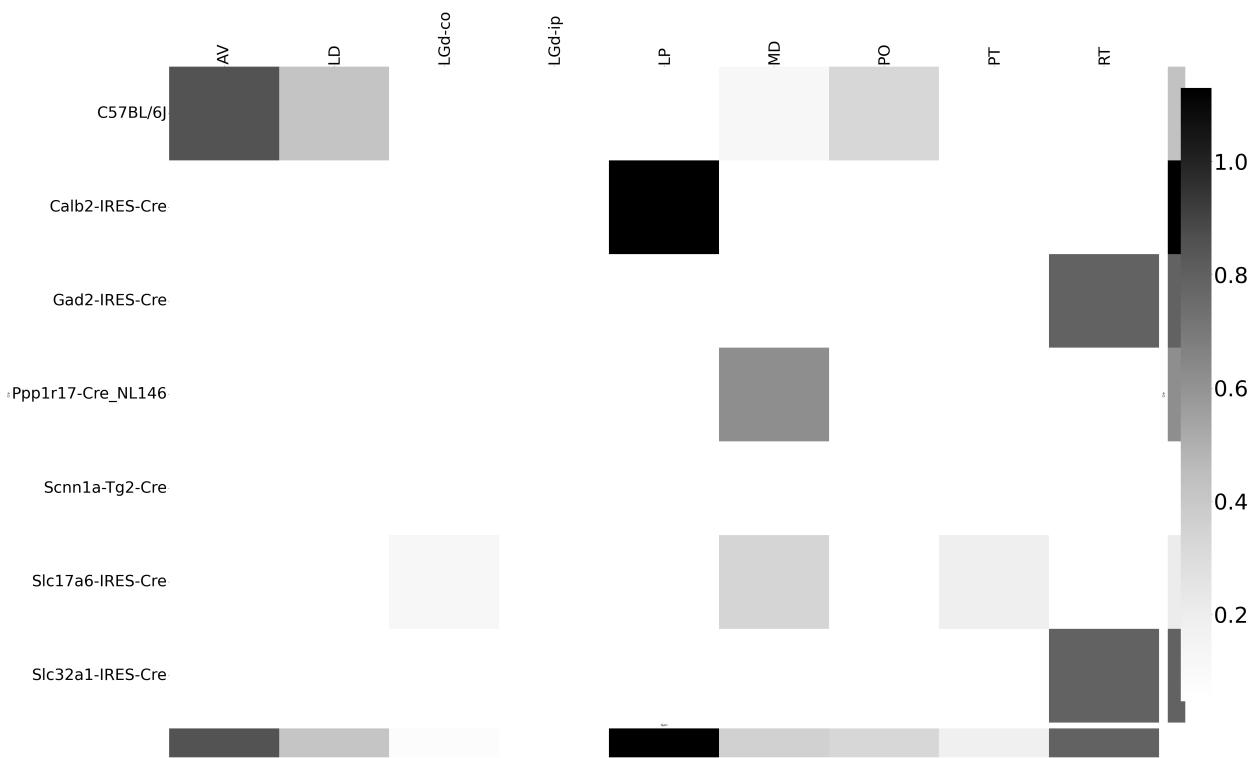


Figure 30: Weighted loss for cre-leaf combinations in TH. Missing values are omitted. Row and column averages are also plotted.

580 **Matrix Factorization**

581 We give additional results on the generation of the archetypal connectome patterns. These consist of  
 582 cross-validation selection of  $q$ , the number of latent components, stability analysis, and visualization  
 583 of the reconstructed wild-type connectivity.

584 *Cross-validation* We set  $\alpha = 0.002$  and run Program 2 on  $\mathcal{C}_{wt}$ . We use a random mask with  $p = .3$  to  
 585 evaluate prediction accuracy of models trained on the unmasked data on the masked data. To  
 586 account for stochasticity in the NMF algorithm, we run  $R = 8$  replicates at each potential dimension  $q$ .  
 587 This selects  $\hat{q} = 60$ .

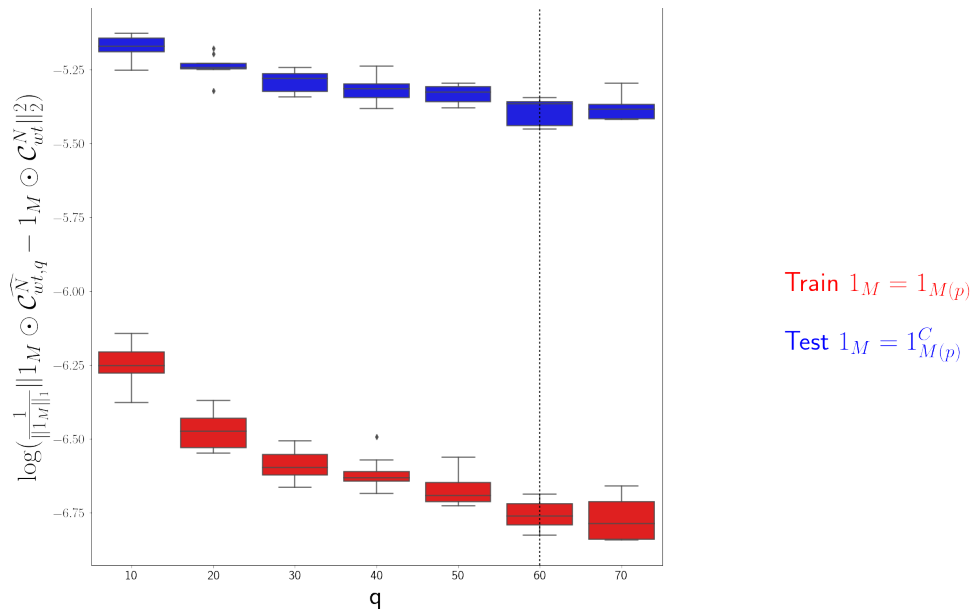


Figure 31: Train and test error using NMF decomposition.

588 *Stability* For the purposes of visualization and interpretability, we restrict to a  $q = 15$  component  
 589 model. To address the instability of the NMF algorithm in identifying components, we  $k - \text{means}$   
 590 cluster components over  $R = 10$  replicates with  $k \in \{10, 15, 20, 25, 30\}$ . Since the clustering is itself  
 591 unstable, we repeat the clustering 25 times and select the  $k$  with the largest Rand index.

592 q	10.000000	20.000000	30.000000	40.000000	50.000000
Rand index	0.772544	0.844981	<b>0.932957</b>	0.929827	0.885862

593 Since  $k$ -means is most stable at  $k = 30$ , we cluster the  $qR = 150$  components into 30 clusters and  
 594 select the 15 clusters appearing in the most replicates.

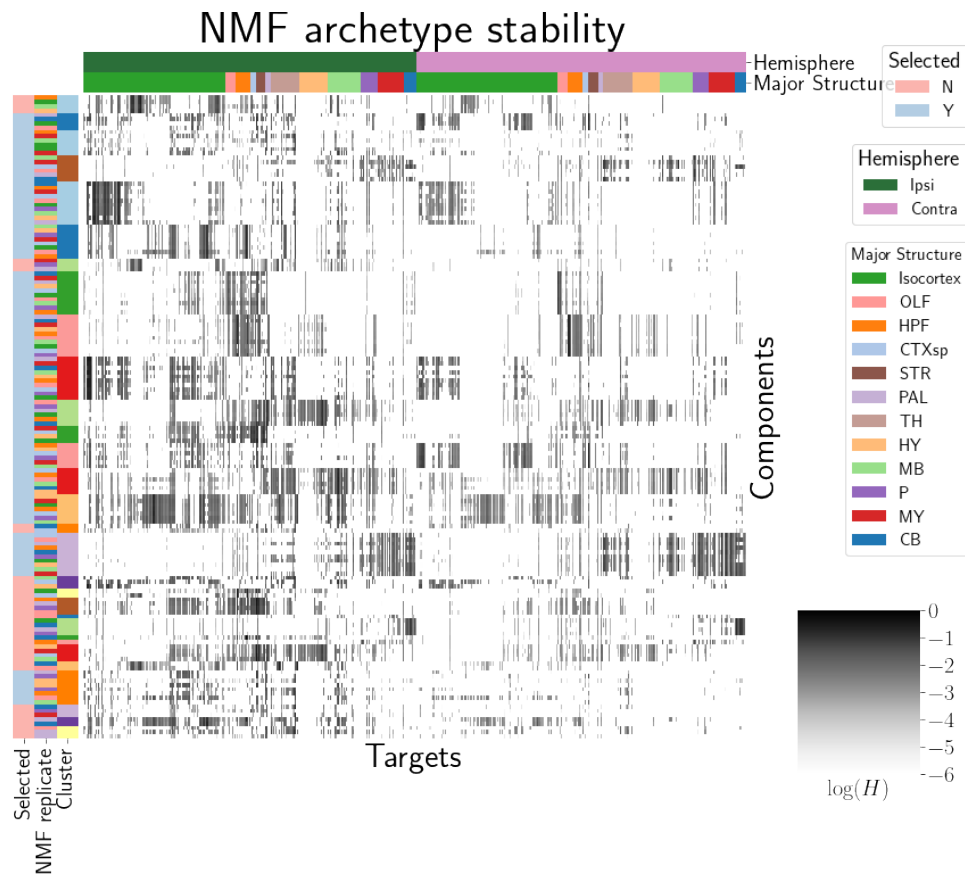


Figure 32: Stability of NMF results across replicates. Replicate and NMF component are shown on rows. Components that are in the top 15 are also indicated.

595 These are the components whose medians are plotted in Figure 4a.

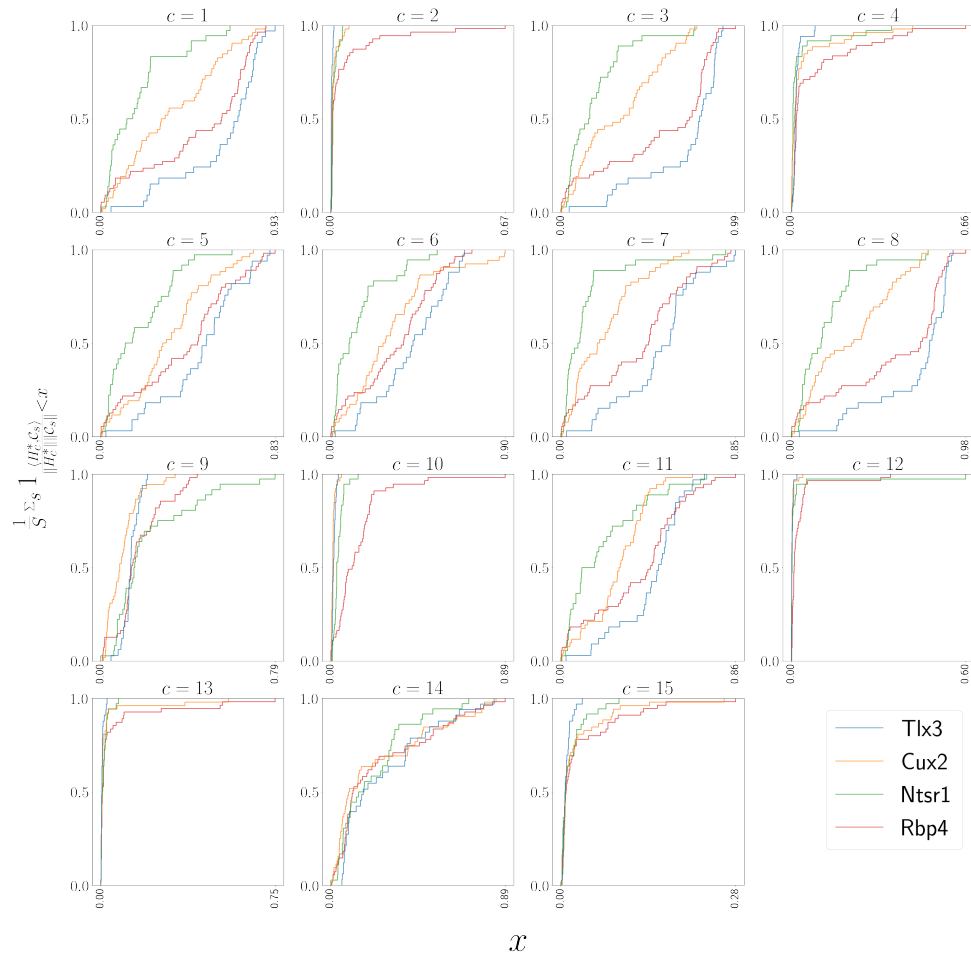


Figure 33: Empirical cumulative distributions of cosine similarities between source structures and connectivity components for four different Cre-lines.

596 *Association with Cre-line*

## 8 COMPETING INTERESTS

<sup>597</sup> This is an optional section. If you declared a conflict of interest when you submitted your manuscript,  
<sup>598</sup> please use this space to provide details about this conflict.

599

600

601

## REFERENCES

- 602 Brunet, J.-P., Tamayo, P., Golub, T. R., & Mesirov, J. P. (2004). Metagenes and molecular pattern discovery using matrix  
603 factorization. *Proc. Natl. Acad. Sci. U. S. A.*, 101(12), 4164–4169.
- 604 Chamberlin, N. L., Du, B., de Lacalle, S., & Saper, C. B. (1998). Recombinant adeno-associated virus vector: use for  
605 transgene expression and anterograde tract tracing in the CNS. *Brain Res.*, 793(1-2), 169–175.
- 606 Daigle, T. L., Madisen, L., Hage, T. A., Valley, M. T., Knoblich, U., Larsen, R. S., ... Zeng, H. (2018). A suite of transgenic  
607 driver and reporter mouse lines with enhanced Brain-Cell-Type targeting and functionality. *Cell*, 174(2), 465–480.e22.
- 608 Gao, Y., Zhang, X., Wang, S., & Zou, G. (2016). Model averaging based on leave-subject-out cross-validation. *J. Econom.*,  
609 192(1), 139–151.
- 610 Harris, J. A., Mihalas, S., Hirokawa, K. E., Whitesell, J. D., Choi, H., Bernard, A., ... Zeng, H. (2019). Hierarchical  
611 organization of cortical and thalamic connectivity. *Nature*, 575(7781), 195–202.
- 612 Harris, J. A., Oh, S. W., & Zeng, H. (2012). Adeno-associated viral vectors for anterograde axonal tracing with fluorescent  
613 proteins in nontransgenic and cre driver mice. *Curr. Protoc. Neurosci., Chapter 1, Unit 1.20.1–18*.
- 614 Harris, K. D., Mihalas, S., & Shea-Brown, E. (2016). Nonnegative spline regression of incomplete tracing data reveals high  
615 resolution neural connectivity.
- 616 Huang, K. W., Ochandarena, N. E., Philson, A. C., Hyun, M., Birnbaum, J. E., Cicconet, M., & Sabatini, B. L. (2019).  
617 Molecular and anatomical organization of the dorsal raphe nucleus. *Elife*, 8.
- 618 Jeong, M., Kim, Y., Kim, J., Ferrante, D. D., Mitra, P. P., Osten, P., & Kim, D. (2016). Comparative three-dimensional  
619 connectome map of motor cortical projections in the mouse brain. *Sci. Rep.*, 6, 20072.
- 620 Knox, J. E., Harris, K. D., Graddis, N., Whitesell, J. D., Zeng, H., Harris, J. A., ... Mihalas, S. (2019). High-resolution  
621 data-driven model of the mouse connectome. *Netw Neurosci*, 3(1), 217–236.
- 622 Kotliar, D., Veres, A., Nagy, M. A., Tabrizi, S., Hodis, E., Melton, D. A., & Sabeti, P. C. (2019). Identifying gene expression  
623 programs of cell-type identity and cellular activity with single-cell RNA-Seq. *Elife*, 8.

- 624 Li, X., Yu, B., Sun, Q., Zhang, Y., Ren, M., Zhang, X., ... Qiu, Z. (2018). Generation of a whole-brain atlas for the  
 625 cholinergic system and mesoscopic projectome analysis of basal forebrain cholinergic neurons. *Proc. Natl. Acad. Sci.*  
 626 *U. S. A.*, 115(2), 415–420.
- 627 Lotfollahi, M., Naghipourfar, M., Theis, F. J., & Alexander Wolf, F. (2019). Conditional out-of-sample generation for  
 628 unpaired data using trVAE.
- 629 Muzerelle, A., Scotto-Lomassese, S., Bernard, J. F., Soiza-Reilly, M., & Gaspar, P. (2016). Conditional anterograde tracing  
 630 reveals distinct targeting of individual serotonin cell groups (B5-B9) to the forebrain and brainstem. *Brain Struct.*  
 631 *Funct.*, 221(1), 535–561.
- 632 Oh, S. W., Harris, J. A., Ng, L., Winslow, B., Cain, N., Mihalas, S., ... Zeng, H. (2014). A mesoscale connectome of the  
 633 mouse brain. *Nature*, 508(7495), 207–214.
- 634 Ren, J., Friedmann, D., Xiong, J., Liu, C. D., Ferguson, B. R., Weerakkody, T., ... Luo, L. (2018). Anatomically defined and  
 635 functionally distinct dorsal raphe serotonin sub-systems. *Cell*, 175(2), 472–487.e20.
- 636 Ren, J., Isakova, A., Friedmann, D., Zeng, J., Grutzner, S. M., Pun, A., ... Luo, L. (2019). Single-cell transcriptomes and  
 637 whole-brain projections of serotonin neurons in the mouse dorsal and median raphe nuclei. *Elife*, 8.
- 638 Saul, L. K., & Roweis, S. T. (2003). Think globally, fit locally: Unsupervised learning of low dimensional manifolds. *J.*  
 639 *Mach. Learn. Res.*, 4(Jun), 119–155.
- 640 Servén D., B. C. (n.d.). *pygam: Generalized additive models in python*.
- 641 von Luxburg, U. (2010a). Clustering stability: An overview.
- 642 von Luxburg, U. (2010b). Clustering stability: An overview.
- 643 Watson, C., Paxinos, G., & Puelles, L. (2012). The mouse nervous system..
- 644 Wu, S., Joseph, A., Hammonds, A. S., Celtniker, S. E., Yu, B., & Frise, E. (2016). Stability-driven nonnegative matrix  
 645 factorization to interpret spatial gene expression and build local gene networks. *Proc. Natl. Acad. Sci. U. S. A.*, 113(16),  
 646 4290–4295.
- 647 Zaborszky, L., Csordas, A., Mosca, K., Kim, J., Gielow, M. R., Vadasz, C., & Nadasdy, Z. (2015). Neurons in the basal  
 648 forebrain project to the cortex in a complex topographic organization that reflects corticocortical connectivity

649 patterns: an experimental study based on retrograde tracing and 3D reconstruction. *Cereb. Cortex*, 25(1), 118–137.

## 9 TECHNICAL TERMS

650 **Technical Term** a key term that is mentioned in an NETN article and whose usage and definition may  
651 not be familiar across the broad readership of the journal.

652 **Cre-line** Refers to the combination of cre-recombinase expression in transgenic mouse and  
653 cre-induced promotion in the vector that induces labelling of cell-class specific projection.

654 **Cell class** The projecting neurons targeted by a particular cre-line

655 **Structural connectivities** connectivity between structures

656 **Voxel** A  $100\mu m$  cube of brain.

657 **Structural connection tensor** Connectivities between structures given a neuron class

658 **dictionary-learning** A family of algorithms for finding low-dimensional data representations.

659 **Shape constrained estimator** A statistical estimator that fits a function of a particular shape (e.g.  
660 monotonic increasing, convex).

661 **Nadaraya-Watson** A simple smoothing estimator.

662 **Connectivity archetypes** Typical connectivity patterns

663 **Expected loss** Our new estimator that weights different features by their estimated predictive  
664 power.